Research Square

Preprints are preliminary reports that have not undergone peer review.
They should not be considered conclusive, used to inform clinical practice,
or referenced by the media as validated information.

Extrachromosomal MYC transactivates GPX4 to restrain ferroptosis and promote radioresistance in lung cancer

lihui xuan
Central South University
jinhua luo
Central South University
huiji pan
Central South University
lin zhu
Central South University
benyang li
Central South University
yongyi wang
Central South University
lei lou
Central South University
ting yuan
Central South University
yujie li
Central South University
pingkun zhou
Academy of Military Medical Sciences
ruixue huang
huangruixue@csu.edu.cn

Central South University

Research Article

Keywords: Extrachromosomal DNA (ecDNA), Ferroptosis, GPX4, MYC amplification, Radiotherapy resistance

Posted Date: November 13th, 2026

DOI: https://doi.org/10.21203/rs.3.rs-11476220/v1

License: This work is licensed under a Creative Commons Attribution 4.0 International License.
Read Full License

Additional Declarations: No competing interests reported.

Extrachromosomal MYC transactivates GPX4 to restrain ferroptosis and promote radioresistance in lung cancer

Lihui Xuan,[1,2] Jinhua Luo,[1,2] Huiji Pan,[1] Lin Zhu,,[1] Benyang Li,[1] Yongyi Wang,[1] Lei Lou,[1]Ting Yuan,[3] Yujie Li,[1] Ping-Kun Zhou,[2]* Ruixue Huang,[1*]

1Xiangya School of Public Health, Central South University, Changsha, Hunan Province 410078, China.
xuanlihui@csu.edu.cn (Lihui Xuan)
luojinhua@csu.edu.cn (Jinhua Luo);
phj944145906@outlook.com (Huiji Pan);
zhuzhulin1999@163.com(Lin Zhu).
256901012@csu.edu.cn (Benyang Li);
770157385@qq.com (Yongyi Wang);
1985025495@qq.com (Lei Lou)
1422391271@qq.com (Yujie Li);

2 Academy of Military Sciences (AMS), Beijing 100850, China. zhoupk@bmi.ac.cn (P.K.Z.)
3 Ting Yuan, Health Management Medical Center, The Third Xiangya Hospital, Central South University, Changsha 410013, China. yuanting@csu.edu.cn(T Y）

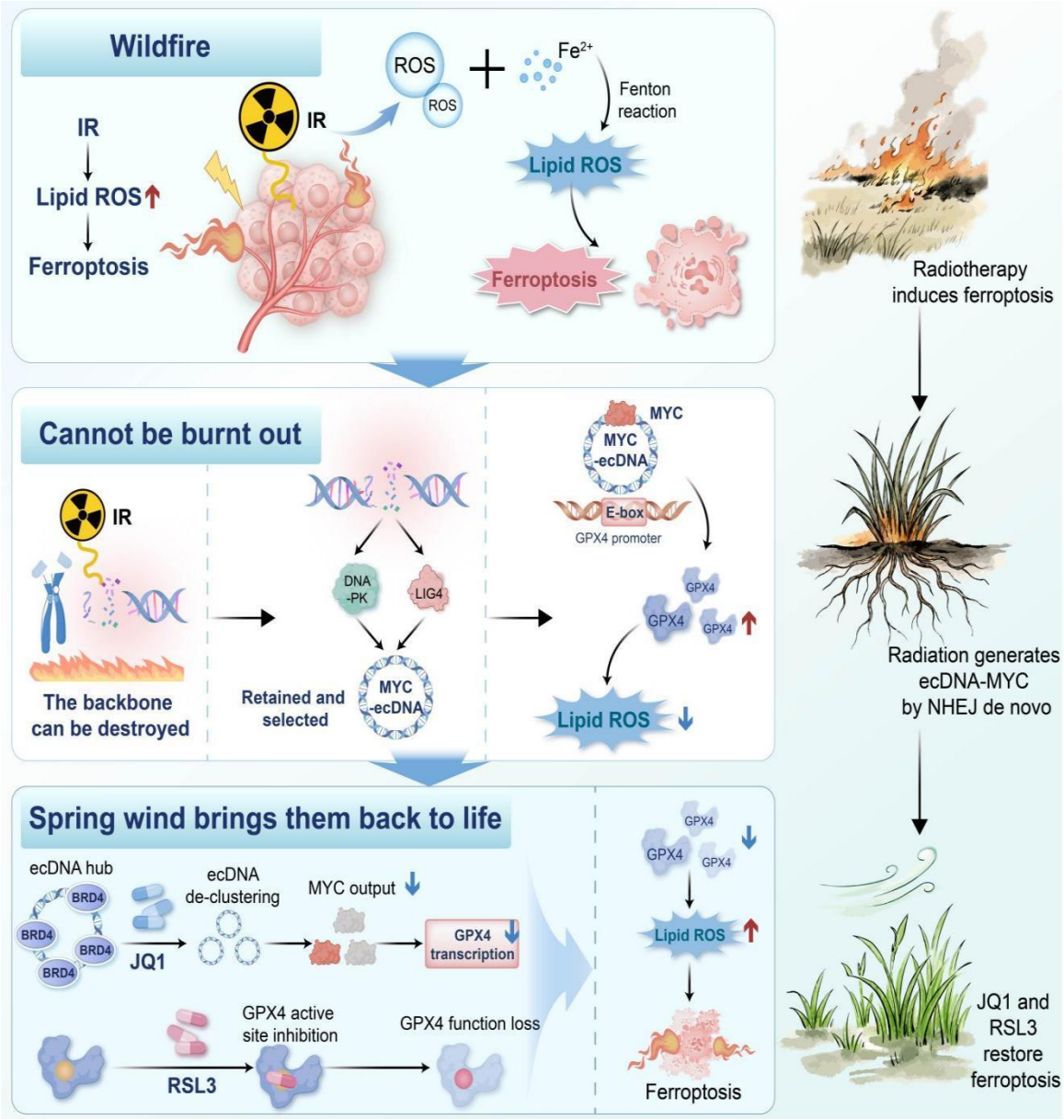
Lead contact
*Correspondence: Ruixue Huang, Ping-kun Zhou
huangruixue@csu.edu.cn (RX.H.),
zhoupk@bmi.ac.cn (P.K.Z.)

Abstract

Purpose:Radiotherapy eliminates tumor cells, in part, by inducing ferroptosis, an iron-dependent form of cell death driven by lipid peroxidation and restrained by glutathione peroxidase 4 (GPX4). However, the mechanisms by which cancer cells suppress ferroptosis and acquire radioresistance remain unclear. Methods and Materials:Using an isogenic model of human bronchial epithelial cells transformed by α-particle irradiation, we demonstrate that ionizing radiation induces de novo formation of MYC-containing extrachromosomal DNA through non-homologous end joining. Results:Extrachromosomal DNA-derived MYC acts in trans on the chromosomal GPX4 locus by binding a canonical E-box within the GPX4 promoter, as demonstrated by ChIP-qPCR, thereby transcriptionally activating GPX4. Disruption of ecMYC, either by BET inhibition or MYC knockdown, abolishes radiation-induced GPX4 upregulation. Elevated GPX4 suppresses radiation-induced lipid peroxidation, establishing an ecMYC-GPX4 transcriptional circuit that promotes radioresistance. Disruption of this circuit or direct inhibition of GPX4 restores ferroptosis and converts radiotherapy from a growth-delaying to a tumor-controlling treatment in xenograft models, with epistasis analysis demonstrating that GPX4 functions downstream of ecMYC. Conclusions:This ecMYC-GPX4 regulatory axis is conserved in A549 lung adenocarcinoma cells and can be monitored non-invasively by Raman spectroscopy, identifying it as a potential therapeutic target for radiosensitization.

Keywords: Extrachromosomal DNA (ecDNA); Ferroptosis; GPX4; MYC amplification; Radiotherapy resistance

Graphic Abstract.



Graphical abstract. The well-known verse, "Wildfire cannot burn them away; they grow again when the spring wind blows," symbolizing the persistence and resurgence of tumor cells despite radiation-induced damage. Mechanistically, ionizing radiation initiates ferroptosis by generating reactive oxygen species (ROS) and Fe^{2+}-dependent Fenton reactions that drive lethal lipid peroxidation. Simultaneously, radiation-induced DNA double-strand breaks are rejoined by the NHEJ machinery (DNA-PK/LIG4), generating MYC-containing ecDNA *de novo*. Following clonal selection, ecDNA-derived MYC binds the E-box within the GPX4 promoter, transcriptionally activating GPX4 expression. Elevated GPX4 detoxifies lipid peroxides, suppresses ferroptosis, and promotes radioresistance. This ecDNA-dependent resistance can be pharmacologically reversed through two complementary approaches:

disruption of ecDNA transcriptional hubs with the BRD4 inhibitor JQ1, which suppresses GPX4 transcription, or direct inhibition of GPX4 enzymatic activity with RSL3. Both strategies restore lipid ROS accumulation and reinitiate ferroptotic cell death. Collectively, these findings identify radiation-induced MYC-containing ecDNA as a key driver of ferroptosis resistance and support BRD4- or GPX4-targeted therapies as promising strategies for resensitizing residual lung cancer cells to radiotherapy.

1. Introduction

Radiotherapy is a key treatment modality for lung cancer; however, its efficacy is limited by intrinsic and acquired radioresistance (Wang et al., 2025). Ionizing radiation has traditionally been considered to eliminate tumor cells primarily by inducing DNA double-strand breaks that culminate in mitotic catastrophe and apoptosis (Patel et al., 2020). More recently, radiotherapy has also been shown to induce ferroptosis, an iron-dependent form of regulated cell death driven by the peroxidation of polyunsaturated membrane phospholipids (Kang et al., 2026). Ferroptosis is antagonized by glutathione peroxidase 4 (GPX4), the only enzyme capable of reducing phospholipid hydroperoxides to their corresponding alcohols, thereby serving as the terminal suppressor of ferroptosis (Chen et al., 2024; Yang et al., 2014). Because radiation-induced tumor cell death is characterized, in part, by oxidative, iron-dependent lipid peroxidation, the mechanisms by which tumors suppress radiation-induced ferroptosis are thought to contribute to clinical radioresistance. However, the mechanisms by which radioresistant lung cancer cells restrain radiation-induced ferroptotic signaling remain incompletely understood.

Extrachromosomal DNA (ecDNA), acentric circular DNA molecules, has emerged as a previously underappreciated but powerful driver of oncogene amplification and genomic rearrangements in cancer (Wong et al., 2026). Previous studies have shown that ecDNA carrying oncogenes, immunoregulatory genes, and enhancers improves transcription of its cargo genes and promotes tumor heterogeneity, thereby accelerating tumor evolution and therapeutic resistance (Yang et al., 2025). Hung et al. demonstrated that ecDNA hubs are tethered by the bromodomain and extraterminal domain protein BRD4 in MYC-amplified colorectal cancer cells, forming a dynamic transcriptional network that may contribute to the acquisition of radiotherapy resistance (Hung et al., 2021). These characteristics have established the ecDNA compartment as an attractive therapeutic target (Tang et al., 2024). Nevertheless, nearly all current knowledge is derived from established tumors, in which ecDNA was investigated as a pre-existing genomic feature.

Two fundamental questions, therefore, remain unresolved. First, where does ecDNA originate? Shoshani et al. used whole-genome sequencing of clonal cancer cells that had acquired chemotherapy resistance to demonstrate that chromothripsis drives circular DNA amplification through mechanisms dependent on PARP and the DNA-dependent protein kinase catalytic subunit (Shoshani et al., 2021). Paradoxically, the DNA damage imposed by radiotherapy may inadvertently promote the acquisition of radioresistance by driving rapid genomic remodeling through chromothripsis and ecDNA evolution. Clinically, however,

ecDNA is predominantly detected as a pre-existing feature that is enriched in advanced or previously treated tumors (Bailey et al., 2024), suggesting selection of existing ecDNA rather than *de novo* generation. It therefore remains unknown whether a defined genotoxic insult, such as clinically relevant ionizing radiation, can directly induce *de novo* ecDNA formation in previously ecDNA-negative cells. Second, does ecDNA intersect with ferroptosis? Despite the central roles of ecDNA in oncogene amplification and of ferroptosis in the radiation response, no functional link has been established between the ecDNA compartment and radioresistance through regulation of the ferroptotic machinery.

Establishing whether ecDNA is generated *de novo* rather than selected requires a model that begins from an ecDNA-negative baseline and undergoes transformation following a defined radiation dose. Here, we used an isogenic model of human bronchial epithelial cells transformed by α-particle irradiation to investigate radiation-induced ecDNA formation (Hei et al., 1996). Because this lineage is initially ecDNA-negative, the emergence of ecDNA can be directly observed rather than inferred from cross-sectional analyses. We demonstrate that ionizing radiation induces the *de novo* formation of MYC-containing ecDNA in a dose-dependent manner. These extrachromosomal elements are heritable and continue to accumulate even during colchicine-induced mitotic arrest. Mechanistically, ecDNA-amplified MYC binds to an E-box within the GPX4 promoter, thereby transcriptionally activating the ferroptosis suppressor GPX4. Consequently, the same radiation that induces lipid peroxidation simultaneously establishes an ecDNA-encoded transcriptional program that counteracts ferroptosis. This regulatory axis is conserved in A549 lung adenocarcinoma cells and patient samples and is fully recapitulated using CRISPR-based circularization (CRISPR-C) of ecMYC. Disrupting ecDNA hubs with BET inhibitors or directly targeting GPX4 with RSL3 abolishes this adaptive protective mechanism, thereby enhancing radiation-induced ferroptosis and restoring tumor control *in vivo*. Finally, this treatment-induced increase in lipid oxidation can be monitored non-invasively using label-free Raman spectroscopy in both tumor tissue and peripheral erythrocytes.

Collectively, these findings redefine ionizing radiation as a direct inducer of ecDNA formation rather than merely a selective pressure that enriches pre-existing ecDNA. They further identify an ecDNA-MYC-GPX4 axis that links oncogene amplification to ferroptosis evasion and radioresistance. Accordingly, lung cancer cells harboring ecMYC exhibit intrinsic radioresistance, but can be resensitized to radiotherapy by targeting either the ecDNA compartment or its downstream ferroptosis suppressor, GPX4. Finally, this study establishes a non-invasive Raman spectroscopy-based strategy for monitoring the ferroptotic

status of patients undergoing radiotherapy.

2. Results

2.1 α-Particle-transformed bronchial epithelial cells acquire dose-dependent radioresistance that is not explained by a generalized drug-tolerant state

Radiotherapy eliminates tumor cells not only through DNA damage-induced apoptosis but also, as is increasingly being recognized, through ferroptosis, an iron-dependent form of cell death driven by lipid peroxidation that is now considered a major mechanism underlying the tumor-suppressive effects of ionizing radiation (Kang et al., 2026). Why some lung tumors evade this form of cell death remains unknown. We reasoned that the mechanisms of radioresistance would be more readily dissected by tracking its emergence within a single genetic background rather than by comparing unrelated tumor cell lines. Therefore, BERP35T1 and BERP35T5, derived from BEP2D cells, were used in this study. BEP2D is an HPV18-immortalized, non-tumorigenic human bronchial epithelial cell line established and characterized in our previous studies (Liu et al., 2025; Liu et al., 2019). Hei et al. reported that BEP2D cells exposed to 1.5 Gy α-particle irradiation from a ^{238}Pu source propagated to passage 35, and when inoculated into nude mice generated tumor-derived cell lines, including BERP35T1 (T1) and BERP35T5 (T5), from the resulting xenografts (Fig. 1a) (Hei et al., 1996; Weaver et al., 1997). Unless otherwise indicated, all subsequent experiments compared BEP2D with T5, the fully transformed derivative.

T5 cells exhibited a more aggressive phenotype than BEP2D across multiple characteristics of malignant transformation. They proliferated more rapidly, as demonstrated both by CCK-8 assays (Fig. 1b) and direct cell counting, with significantly higher cell numbers at 48 h and 72 h, but not at 24 h (Fig. 1c). T5 cells also displayed approximately 11-fold greater clonogenic capacity (Fig. 1d), achieved approximately 3.6-fold faster wound closure at 12 h in scratch assays (Fig. 1e, f), and exhibited approximately 2.9-fold greater invasiveness in Transwell assays (Fig. 1h). Given that the two cell lines showed comparable cell numbers at 24 h (Fig. 1c), the enhanced wound closure observed at 12 h reflected increased migratory capacity rather than proliferation. We next used clinically relevant low-linear energy transfer ^{60}Co γ-rays to investigate whether malignant transformation in this lineage is accompanied by altered radiosensitivity. Colony formation declined as the radiation dose increased in both cell lines, but the reduction was significantly greater in BEP2D than in T5 (Fig. 1g, i). Although survival was comparable at 2 Gy, a marked divergence emerged at 8

Gy, indicating a radioresistant phenotype that was minimal at low doses but became pronounced with increased radiation exposure. Short-term viability assays across 0–14 Gy yielded consistent results, with T5 cells maintaining significantly higher viability at doses of 4 Gy and above (Fig. 1j). These findings indicate that radioresistance emerged concomitantly with malignant transformation in this model.

Temozolomide, the cytotoxicity of which is mediated primarily through O^6-methylguanine mispairing and is largely independent of redox status, produced nearly identical dose–response curves in both cell lines (Fig. 1l), excluding the presence of a generalized, agent-independent drug-tolerant phenotype. Cisplatin induced only a modest rightward shift in the dose–response curve of T5 cells (Fig. 1k). Together, these findings argue against a classical multidrug-resistant phenotype and instead suggest a resistance mechanism specific to agents that induce oxidative, membrane-directed damage, with ionizing radiation representing the most potent example. We therefore sought to identify a protective mechanism that counteracts oxidative membrane damage rather than DNA adduct formation.

γ-irradiation reduced cell viability (Fig. S1a) and induced a dose-dependent accumulation of propidium iodide-positive, membrane-permeabilized cells (Fig. S1, b and c), whereas Annexin V-positive cells remained a minor population even at 8 Gy (Fig. S1, d and e). This dissociation was consistent with the biology of this cell lineage. BEP2D cells and their derivatives express HPV18 E6/E7 and are functionally deficient in p53, resulting in constitutive suppression of the p53-dependent apoptotic response to radiation. Because this defect is shared by both parental and transformed cells, it cannot account for their differential radiosensitivity. Instead, the persistence of membrane-permeabilizing cell death suggests the involvement of a non-apoptotic, membrane-destructive mechanism. Furthermore, both cisplatin and temozolomide induced dose-dependent C11-BODIPY oxidation in BEP2D and T5 cells (Fig. S2 and S3), demonstrating that this probe reliably detects lipid peroxidation in the present model and that both cell lines retain the capacity to oxidize membrane phospholipids. These findings raise the central question addressed in this study: what is the genomic alteration that enables radiation-transformed bronchial epithelial cells to restrain the lipid peroxidation induced by ionizing radiation itself?

2.2 Circle sequencing identifies radiation-induced circular DNA at the MYC and GPX4 loci

EcDNA is a pervasive vehicle for focal oncogene amplification, which drives aggressive disease and poor clinical outcomes across multiple cancer types (Yan et al., 2024). Its circular topology can be captured genome-wide using circle-enrichment sequencing. We applied this approach to identify the genomic loci that undergo circularization during radiation-induced transformation. The extrachromosomal circular DNA landscape was profiled in BEP2D, T5, and T5 cells re-challenged with a single 8 Gy dose of X-rays. Genomic DNA was enriched in circular species by alkaline denaturation, mitochondrial DNA was linearized using MssI, residual linear DNA was removed with Plasmid-Safe ATP-dependent DNase, and the remaining circular DNA was amplified by φ29 rolling-circle amplification before sequencing (Illumina NovaSeq 6000, PE150). Circular DNA molecules were identified using Circle-Map (split reads ≥ 1) (Fig. 2a, b).

In these libraries, MYC was detected as circular DNA in T5 but not in BEP2D, with a prominent peak (Peak40964) that clearly exceeded the background observed in BEP2D (Fig. 2c). Because the recovered circles were predominantly 250–500 bp in length (Fig. 2d), circle sequencing reflected circularization events rather than the absolute size of ecDNA elements. We therefore used the co-amplified MYC locus as a tractable reporter to investigate the extrachromosomal nature, dose dependence, and heritability of radiation-induced amplification, while returning to GPX4 below as the functionally critical transcriptional target. High-confidence circular DNA counts increased approximately 2.5–3-fold from BEP2D to T5 and increased further following irradiation of T5 cells (T5+IR) (Fig. 2e). The proportion of the genome represented within circular DNA showed the same trend (Fig. 2f). Newly gained circles were predominantly derived from protein-coding regions, with lncRNAs, pseudogenes, and multi-biotype elements comprising the remainder (Fig. 2g), whereas lost circles displayed a broadly similar composition (Fig. 2h). Most circularized sequences mapped to exonic and intronic regions (Fig. 2i), indicating that radiation preferentially induced circularization within transcriptionally active, gene-dense chromatin. The genes contained within gained circles were enriched in pathways related to focal adhesion, Rap1 signaling, estrogen signaling, chemokine signaling, axon guidance, and actin cytoskeleton organization (Fig. 2j).

Among these differentially circularized loci, one was particularly notable. On chromosome 19p13.3, a prominent circular DNA peak (Peak40964) spanning the GPX4 locus (gene order: ARHGAP45-POLR2E-GPX4-SBNO2) was virtually absent in BEP2D but strongly detected in T5 cells (Fig. 2b, f). GPX4 is the only glutathione-dependent enzyme that reduces phospholipid hydroperoxides to their corresponding alcohols and, therefore, functions

as the terminal suppressor of ferroptosis downstream of system xc^- (SLC7A11/SLC3A2)-mediated cystine uptake and glutathione synthesis (Fig. 2k). Quantitative RT-PCR analysis of ferroptosis-related genes demonstrated coordinated induction following 8 Gy irradiation of the antioxidant/cystine import module (SLC7A11), the glycolysis-lactate module (LDHA and SLC16A1), MYC, and the canonical ferroptosis marker PTGS2/COX2, together with altered expression of ACSL4, TP53, and AARS1 (Fig. S4). Because circle sequencing provides a population-averaged measure of circular DNA topology, we next sought single-cell cytogenetic evidence that this amplified compartment was truly extrachromosomal using the co-amplified MYC locus as a tractable reporter.

2.3 MYC amplification in radiation-transformed cells is extrachromosomal and scales with radiation dose

A defining characteristic of ecDNA is that amplified oncogenes reside on centromere-deficient extrachromosomal bodies (double minutes) that segregate unequally during mitosis, a feature most directly visualized at the single-cell level by DNA fluorescence *in situ* hybridization (DNA FISH) (Song et al., 2026). Because MYC was identified as circular DNA together with GPX4, we used it as a single-cell reporter of the extrachromosomal compartment. Two-color DNA FISH was performed using an MYC probe (red) and a chromosome 8 centromere enumeration probe (CEP8, green). In BEP2D cells, both metaphase spreads and interphase nuclei displayed few MYC signals, each colocalizing with a CEP8 signal and matching CEP8 copy number, consistent with a chromosomal MYC locus. In contrast, T1 and T5 cells exhibited numerous MYC signals scattered throughout the nucleoplasm, which appeared in metaphase spreads as small acentric bodies independent of any chromosome. Accordingly, MYC copy number significantly exceeded CEP8 copy number (Fig. 3a).

Irradiation increased extrachromosomal MYC (hereafter ecMYC) in a dose-dependent manner. In both T1 and T5 cells, interphase nuclei and metaphase spreads accumulated increasing numbers of free MYC foci as the radiation dose increased from 0 to 2 to 8 Gy (Fig. 3e, T1; Fig. 3g, T5). In T5 cells, this effect was quantified, demonstrating a stepwise increase in MYC foci per cell with increasing radiation dose (Fig. 3i). Because these amplified elements were acentric double minutes rather than contiguous intrachromosomal amplicons, and because CEP8 copy number remained unchanged, chromosome 8 polysomy and intrachromosomal high-level amplification (HSR-like amplification) can be excluded as the

source of the additional MYC copies. Notably, this radiation-induced increase was specific to the MYC amplicon. Total extrachromosomal circular DNA per cell did not increase, remaining unchanged in T1 cells (Fig. 3f) and decreasing in T5 cells (Fig. 3h). Following exposure to 8 Gy, ecMYC was visibly more abundant in the radiation-transformed clones than in BEP2D cells (Fig. 3j). Quantitative analysis confirmed that T5 cells harbored significantly more c-Myc foci than did BEP2D cells in both metaphase (Fig. 3k) and interphase nuclei (Fig. 3l), whereas the lung adenocarcinoma cell line A549 displayed an intermediate phenotype (Fig. 3k). This extrachromosomal amplification translated into increased oncogene expression. MYC mRNA levels were markedly elevated in T5 and A549 cells compared to BEP2D cells (Fig. 3m), and c-Myc protein expression was similarly increased in T5 and A549 cells relative to BEP2D cells (Fig. 3n, o). As demonstrated in the following sections, this proportional increase in MYC dosage provides the mechanistic link between the ecDNA compartment and regulation of the ferroptosis machinery.

2.4 Radiation-born ecDNA requires non-homologous end joining, depends on BET/BRD4 hubs, and is heritable

EcDNA is thought to arise from catastrophic DNA double-strand break (DSB) events, such as chromothripsis and breakage-fusion-bridge cycles (Kadali and Shoshani, 2025; Shoshani et al., 2021), and, once formed, its transcriptional activity depends on BRD4-containing hubs that cluster ecDNA molecules (Nichols et al., 2025). We investigated whether radiation-induced ecDNA follows these principles and how it is maintained across successive cell divisions. Because circularization of DSB ends is expected to require classical non-homologous end joining (NHEJ), we examined whether inhibition of the two rate-limiting NHEJ components, DNA-dependent protein kinase (DNA-PK), which initiates NHEJ, and DNA ligase IV (LIG4), which mediates terminal ligation, suppresses ecMYC formation. Inhibition of either DNA-PK or LIG4 significantly reduced the number of ecMYC foci (Fig. 4a–c), whereas the number of CEP8 signals in the same metaphase spreads remained unchanged. Two additional agents used as orthogonal perturbations, an LSD1 inhibitor and 5-fluorouracil, also reduced ecMYC levels, although neither directly tests the NHEJ hypothesis. The dependence on DNA-PK and LIG4 places NHEJ-mediated end joining upstream of radiation-induced ecDNA formation and may explain why ionizing radiation, a potent physical inducer of DSBs, efficiently generates ecDNA.

Because ecDNA clustering and transcriptional activity depend on BRD4-containing hubs (Nichols et al., 2025), we next evaluated the BET bromodomain inhibitor JQ1. JQ1 reduced the number of extrachromosomal MYC foci in metaphase T5 and A549 cells (Fig. 4d, e), consistent with depletion of the ecMYC compartment. Thus, JQ1 provides a tractable pharmacological strategy for reducing the ecMYC burden.

Finally, we investigated the heritability of radiation-induced ecDNA. In colchicine-arrested metaphase cells, ecMYC was readily visualized as clustered extrachromosomal bodies (Fig. 4f, g), and it remained abundant after serial passaging and re-preparation of metaphase spreads (Fig. 4h), indicating that ecMYC is stably retained through successive mitotic divisions. Because our isogenic model originates from ecDNA-negative bronchial epithelial cells (BEP2D) and acquires ecMYC only after irradiation, the ecDNA observed here must arise *de novo* in response to radiation rather than through selection of a pre-existing ecDNA population, identifying ionizing radiation itself as a direct driver of ecDNA biogenesis. To characterize the inherited species, we performed junction-specific qPCR across serial passages. From IR-P0 to IR-P4, the divergent junction signal remained consistently elevated in irradiated cells relative to controls (Fig. 4i), whereas exon-internal copy number remained unchanged. This junction-specific signature indicates that the heritable species is the circularized locus rather than an increase in chromosomal copy number, although exonuclease resistance assays or junction sequencing would be required to formally exclude tandem duplication junctions. The associated phenotype was similarly maintained. Expression of COX2 (PTGS2), a canonical ferroptosis marker, remained elevated throughout all irradiated passages (Fig. 4j), indicating that inheritance of ecMYC is accompanied by a persistent ferroptosis-associated transcriptional state.

2.5 Radiation elicits mitochondria-weighted lipid peroxidation that is restrained below the ferroptotic threshold by a compensatory GPX4 response

Having demonstrated that radiation induces heritable MYC-containing ecDNA with co-amplification of the GPX4 locus, we next investigated how these cells simultaneously generate and survive extensive lipid peroxidation. Irradiation induced the characteristic morphological features of ferroptosis, accompanied by loss of plasma membrane integrity (Fig. 5a). Redox-sensitive C11-BODIPY imaging and quantitative analysis revealed a dose-dependent increase in oxidized probe fluorescence (Fig. 5b, c), which was reproduced in independent experiments using the non-oxidized fluorescence channel as a specificity control

(Fig. S6 and S7). Malondialdehyde, a terminal product of lipid peroxidation, increased in parallel (Fig. 5d). These findings demonstrate that radiation activated the ferroptotic execution pathway and produced the strongest lipid peroxidation signal in the most highly transformed cell line.

GPX4 provides a mechanistic explanation for how these cells tolerate this oxidative stress. Immunoblot analysis of BEP2D, T1, and T5 cells following exposure to 0, 2, or 8 Gy showed that basal GPX4 expression was markedly higher in the transformed cell lines than in BEP2D and increased further in a dose-dependent manner after irradiation, paralleling the induction of c-Myc and the ferroptosis marker PTGS2 (COX-2) (Fig. 5e, f; replicated in Fig. S8). GPX4 immunofluorescence confirmed the same expression pattern, with the strongest staining observed in T5 cells and progressive increases with radiation dose (Fig. 5g–i). Thus, radiation-transformed cells mount a compensatory, dose-dependent GPX4 response that counteracts the lipid peroxidation induced by ionizing radiation. We refer to this state as GPX4-restrained ferroptosis, in which lipid peroxidation is robustly induced but ferroptotic cell death is prevented from reaching its execution threshold.

2.6 Suppression of ecDNA-MYC signaling releases radiation-induced ferroptosis

Because ecDNA copy number is subject to strong dynamic selection and its transcriptional activity depends on BRD4-organized ecDNA hubs (Hung et al., 2021; Lange et al., 2022), we investigated whether disrupting this output converts sublethal GPX4-restrained lipid peroxidation into overt ferroptosis. Using si-c-Myc-mediated transcript knockdown and the BET bromodomain inhibitor JQ1, either alone or in combination with 8 Gy irradiation (Fig. 5j–l), we found that neither intervention alone was strongly cytotoxic, whereas irradiation alone induced only moderate lipid peroxidation. In contrast, both si-c-Myc + IR and JQ1 + IR markedly enhanced radiation-induced lipid peroxidation (Fig. 5k). Flow cytometric quantification of oxidized C11-BODIPY confirmed this increase (Fig. 5m, n), while JQ1 also reduced the numbers of scattered ecMYC FISH foci in irradiated T5 cells (Fig. 5l), directly linking depletion of the ecDNA compartment to radiosensitization. This effect was reproduced using mechanistically distinct interventions that either suppressed MYC/ecDNA output or augmented genotoxic stress. JQ1, an LSD1 inhibitor, and 5-fluorouracil each enhanced lipid peroxidation when combined with 8 Gy irradiation, with the combination of JQ1 and irradiation producing the strongest effect (Fig. S9). Dual-laser imaging further localized a substantial proportion of the lipid peroxidation signal to the

mitochondrial network, a pattern that increased with radiation dose specifically in T5 cells (Figs. S10 and S11). These findings indicate that radiation-induced ferroptosis in transformed cells is limited not by insufficient ferroptotic signaling but by an ecDNA-dependent protective mechanism, and that disrupting this defense releases the ferroptotic brake.

2.7 MYC, including its ecDNA-borne circular form, directly transactivates GPX4 through a promoter E-box

On ecDNA, co-amplified regulatory elements and transposable element-derived enhancers can reprogram oncogene transcription, and ecDNA-borne enhancers have been shown to drive MYC expression. We therefore asked the reciprocal question: does the MYC produced from radiation-induced ecDNA directly activate the ferroptosis suppressor GPX4? Ectopic expression of c-Myc in BEP2D cells (BEP2D-h-c-Myc) was sufficient to increase both GPX4 protein (Fig. 6a, b) and mRNA expression (Fig. 6c). Likewise, expression of circular ecMYC increased GPX4 protein (Fig. 6d, e) and transcript levels (Fig. 6f), demonstrating that MYC in its native circular configuration is fully competent to activate GPX4 transcription.

Mechanistically, the GPX4 promoter contains a canonical E-box matching both the MYC consensus motif (JASPAR MA0147.4, CCACGTGC) and the MAX::MYC binding motif (MA0059.2, ACCACGTGGT) (Fig. 6g). GPX4 expression activity decreased post JQ1 or siMYC treatment (Fig. 6h). MYC ChIP-qPCR demonstrated strong and specific enrichment at this E-box relative to the IgG control, with no enrichment detected in a negative-control region (Fig. 6i). Consistently, MYC ChIP revealed a distinct occupancy peak centered around the GPX4 transcription start site (−300 to +300 bp; Fig. 6j). These findings establish GPX4 as a direct transcriptional target of MYC.

We next examined whether radiation-induced GPX4 upregulation depends on ecMYC. Irradiation increased both c-MYC and GPX4 protein expression and altered the expression of downstream ferroptosis-related markers, including ACSL4, PTGS2, SLC7A11/xCT, and CHAC1. Both JQ1 treatment and si-c-Myc abolished radiation-induced c-MYC and GPX4 expression at both 2 and 8 Gy (Fig. 6k–l), and similar suppression was observed throughout a 12-, 24-, and 48-h JQ1 treatment time course (Fig. S12). GPX4 immunofluorescence in both untreated and irradiated T5 cells was likewise markedly reduced by JQ1 treatment (Fig. 6m, n, o). This regulatory circuit was conserved in an independent, unmanipulated cell line. In A549 cells, JQ1 reduced GPX4 immunofluorescence as well as both c-MYC and GPX4 protein

expression (Fig. S13), indicating that the ecDNA-MYC-GPX4 regulatory axis is not unique to the BEP2D-derived model. Fig.p, q showed clonogenic rate decreased in T5 cells treated with 500 nM JQ1 with 2 or 8 Gy. Fig.r, s showed clonogenic rate decreased in T5 cells treated with si-c-Myc, with 2 or 8 Gy. n. Fig.t, u showed cell viability (CCK-8) under the corresponding JQ1 and si-c-Myc conditions.Fig.v showed representative ferrous-iron probe fluorescence images of T5, T5+JQ1, T5-IR and T5-IR+JQ1 cells. Scale bar, 20 μm.Fig.w showed (w) Quantification of ferrous-iron fluorescence intensity (T5-0Gy vs T5-JQ1, not significant; T5-IR, $P < 0.0001$; T5-IR+JQ1, $P = 0.0001$).

To evaluate the extrachromosomal configuration specifically, we used CRISPR-C to excise and circularize the endogenous MYC locus. Paired Cas9-gRNA ribonucleoprotein complexes generated DNA breaks approximately 2.9 kb upstream and 5.2 kb downstream of MYC, and religation of the liberated ~15.7 kb fragment produced circular ecMYC, while the flanking chromosomal ends rejoined to generate an edited linear allele. Formation of the circular junction was confirmed by junction-spanning PCR, 100% identity Sanger sequencing, and junction-specific qPCR (Fig. S14).

Together with the Circle-seq and DNA FISH data, these findings define a compensatory, radiation-induced regulatory circuit. Ionizing radiation generates NHEJ-dependent MYC-containing ecDNA *de novo*, with concurrent circularization of the GPX4 locus. The resulting extrachromosomal MYC binds the E-box within the GPX4 promoter and directly activates GPX4 transcription. Elevated GPX4 subsequently suppresses the lipid peroxidation induced by the same radiation stimulus, thereby establishing a self-limiting feedback loop that promotes radioresistance (Fig. 2k).

2.8 Targeting ecDNA restores radiation-induced ferroptosis and tumor control *in vivo*

EcDNA-positive tumors evade therapy in part through rapid copy number plasticity, and the ecDNA compartment has emerged as a promising therapeutic vulnerability. We first evaluated this regulatory circuit in cultured cells and subsequently in subcutaneous xenograft models using two complementary epistasis-based experimental designs. *In vitro*, the experimental groups comprised Control, h-c-Myc, RSL3, IR, IR + h-c-Myc, and IR + h-c-Myc + RSL3, enabling direct resolution of the functional relationship between the two regulatory nodes (Fig. 7a). Irradiation shifted the C11-BODIPY probe toward its oxidized form, whereas ectopic c-Myc expression largely suppressed this radiation-induced oxidation, consistent with MYC providing a GPX4-dependent protective mechanism. Addition of the

GPX4 inhibitor RSL3 to the IR + h-c-Myc group abolished this protection and restored the oxidized signal to its maximal level. Thus, MYC-mediated protection against radiation-induced lipid peroxidation requires GPX4 activity, placing GPX4 functionally downstream of MYC.

We next investigated whether the same regulatory hierarchy operates *in vivo* and whether the ecDNA compartment responsible for MYC amplification represents a therapeutically targetable vulnerability. T5 xenografts were established in nude mice and randomly assigned to five treatment groups: untreated control (Con), irradiation alone (IR), the BET inhibitor JQ1 alone (JQ1), JQ1 combined with irradiation (JQ1 + IR), and a rescue group in which GPX4 was re-expressed on the JQ1 + IR background (JQ1 + IR + OEGPX4) (Fig. 7b). Tumors from all five groups were excised and photographed at the experimental endpoint (Fig. 7c). Hematoxylin and eosin staining demonstrated treatment-dependent alterations in tumor architecture, with the JQ1 + IR group exhibiting the greatest loss of viable tumor parenchyma, whereas the rescue group reverted toward the histological appearance observed following irradiation alone (Fig. 7d). Tumor growth measurements showed the same pattern (Fig. 7e).

The biochemical findings closely paralleled the histological observations. Intratumoral 4-hydroxynonenal (4-HNE), a stable aldehyde adduct generated during lipid peroxidation, remained low in the Con, IR, and JQ1 groups, increased markedly following combined JQ1 + IR treatment, and declined after GPX4 re-expression (Fig. 7f). FISH analysis of GPX4 locus-associated ecDNA foci in tumor sections confirmed that JQ1 effectively targets the ecDNA compartment *in vivo* and that the GPX4 locus is carried on this ecDNA (Fig. 7g). Intratumoral malondialdehyde (MDA), another terminal product of lipid peroxidation, exhibited an identical pattern (Fig. 7h). Representative immunohistochemical staining for 4-HNE and c-MYC across all five treatment groups is provided in Figs. S15 and S16. These findings demonstrate that irradiation alone delays tumor growth without inducing complete tumor eradication, consistent with a GPX4-restrained ferroptotic state. In contrast, disruption of the ecDNA compartment converts the same radiation dose into a ferroptosis-executing treatment, whereas restoration of GPX4 expression alone, downstream of the molecular events disrupted by JQ1, is sufficient to re-establish therapeutic resistance. Thus, depletion of ecDNA converts radiotherapy from a growth-delaying intervention into an effective tumor-controlling treatment *in vivo*, with GPX4 representing the critical downstream effector of this transition.

To determine whether this regulatory circuit can be detected in a label-free manner at the single-cell level, we performed confocal Raman spectroscopy on T5 cells under two experimental conditions: ecDNA hub disruption followed by irradiation (JQ1 + IR) and the same treatment combined with GPX4 re-expression (JQ1 + IR + OEGPX4) (Fig. 7i, j). Three spectral features were extracted from each single-cell Raman spectrum: the lipid CH_2 bending mode (1440–1450 cm^{-1}), reflecting total lipid content; a carbonyl/C=C band (~1650–1740 cm^{-1}), attributable to the α,β-unsaturated aldehydes generated during lipid peroxidation and used here as a label-free surrogate for 4-HNE; and the C–H stretching intensity ratio I_{2930}/I_{2850} (2850–2930 cm^{-1}), which reflects changes in the protein-to-lipid signal and the acyl-chain disorder associated with lipid peroxidation. Compared to JQ1 + IR + OEGPX4 cells, JQ1 + IR cells exhibited significantly higher carbonyl/4-HNE-associated signals and a significantly elevated I_{2930}/I_{2850} ratio, indicating that GPX4 re-expression altered the oxidative state of membrane lipids rather than their overall abundance (Fig. 7i). Raman imaging of the corresponding fields further demonstrated that oxidized lipid signals appeared as bright intracellular foci in JQ1 + IR cells but were largely abolished following GPX4 re-expression (Fig. 7j).

2.9 Raman spectroscopy detects the ecDNA-GPX4-ferroptosis axis in cells, tumors, and patient blood

We next asked whether the same lipid-peroxidation signature distinguishes radiosensitive from radioresistant human lung tumors at the tissue level. Confocal Raman maps were acquired from resection specimens of radiosensitive and radioresistant lung cancers. Maps were quantified after normalization at 851 cm^{-1} (proline/hydroxyproline ring breathing, collagen-associated), 1090 cm^{-1} (PO_2^- symmetric stretch, contributed by nucleic acids and phospholipids), 1440–1450 cm^{-1} (lipid CH_2 bending), 2850–2860 cm^{-1} (lipid CH_2 symmetric stretching) and 2932 cm^{-1} (protein CH_3 stretching). GPX4, 4-HNE and MDA were instead assessed on serial sections imaged in the matched tumor region (Fig. 8a). Radiosensitive tumors showed higher 4-HNE and MDA staining together with lower GPX4 signal, whereas radioresistant tumors showed the opposite pattern; the corresponding Raman band intensities differed in the same direction (Fig. 8b).

We then asked whether this state could be detected non-invasively in peripheral blood. Because circulating erythrocytes are rich in membrane lipids, carry abundant heme, and are highly susceptible to oxidative damage, we reasoned that systemic oxidative stress might leave a detectable spectral signature in these cells. Label-free Raman spectra of individual erythrocytes were acquired at [λ] nm from three age- and sex-matched groups: healthy donors (Control, n = 27), treatment-naive patients with lung cancer (Tumor, n = 28) and patients sampled weeks after completion of thoracic radiotherapy (Tumor + IR, n = 30). Blood was

processed of venipuncture and samples were measured in randomized order within a single batch-controlled workflow (Fig. 8c). After quality control and preprocessing, 4,150 single-cell spectra from 85 evaluable donors entered the analysis.

To avoid pseudoreplication, group comparisons used the per-donor mean spectrum as the unit of analysis. Intensities at each of the analysed Raman shifts were compared by Kruskal–Wallis test with Dunn post-hoc comparison, and P values were corrected across all shifts by the Benjamini–Hochberg procedure (FDR < 0.05) (Fig. 8d), with assignments based on Movasaghi et al. (2007) and on established hemoglobin Raman assignments. In unsupervised analyses, spectra from the three groups overlapped substantially in t-SNE (Fig. 8e), indicating that group identity is not the dominant axis of unsupervised variance. Supervised linear discriminant analysis, in contrast, resolved the three groups (Fig. 8f). The MLP classified individual spectra with sensitivities of 84.33% (Control), 85.33% (Tumor) and 68.67% (Tumor + IR) (Fig. 8g, h) and one-vs-rest AUCs of 0.94, 0.91 and 0.92 (Fig. 8i).

Together, these findings show that label-free Raman spectroscopy of peripheral erythrocytes distinguishes healthy individuals, patients with lung cancer and patients after radiotherapy, and that the discriminating features are heme oxidation-state and globin conformational modes consistent with systemic oxidative stress.

3. Discussion

Radioresistance remains the principal barrier to curative radiotherapy for lung cancer, and the mechanisms by which tumor cells survive a treatment now known to induce ferroptosis remain incompletely understood. Using an isogenic model in which normal human bronchial epithelial cells undergo progressive transformation following α-particle irradiation, we demonstrated that ionizing radiation induces *de novo* formation of ecDNA through NHEJ. We further showed that this ecDNA carries MYC as a dose-dependent, heritable extrachromosomal element verified at the single-cell level; that ecDNA-derived MYC binds the GPX4 promoter E-box and directly transactivates the ferroptosis suppressor GPX4; and that the resulting GPX4-restrained ferroptotic state underlies radioresistance and can be reversed *in vivo* by either depleting ecDNA or inhibiting GPX4.

Our most unexpected finding concerns the origin of ecDNA. Most existing evidence, derived from large cross-sectional studies, indicates that ecDNA is already present in tumors and becomes increasingly prevalent in advanced and previously treated cancers (Bailey et al., 2024; Kim et al., 2020). These observations have generally been interpreted as reflecting selection of pre-existing, high-copy ecDNA clones under therapeutic pressure (Bailey et al., 2024). In contrast, our isogenic model begins from an ecDNA-negative baseline, and ecMYC continues to accumulate even when mitosis is blocked by colchicine, demonstrating that the

observed ecDNA is generated *de novo* rather than selected. Mechanistically, this finding is consistent with a previous study showing that chromothripsis drives circular DNA amplification through a DNA-dependent protein kinase catalytic subunit-dependent process (Shoshani et al., 2021). Accordingly, we demonstrate that radiation-induced ecDNA biogenesis requires both DNA-PK and DNA ligase IV, two core components of the NHEJ pathway. Thus, while our findings support the prevailing view that double-strand break repair machinery is essential for ecDNA formation, they extend this concept by identifying a defined and clinically relevant genotoxic stimulus—ionizing radiation—as a direct inducer of ecDNA biogenesis in previously normal bronchial epithelium. These findings reconcile the apparent discrepancy between ecDNA generation and therapeutic selection by suggesting that they represent sequential processes: radiation first generates ecDNA, whereas subsequent treatment selects for ecDNA-containing clones. Cross-sectional tumor studies, therefore, capture the cumulative outcome of both processes, whereas our time-resolved isogenic model isolates the initial generative event.

A second important point concerns the mechanism by which ecDNA exerts its biological effects. Recent studies have demonstrated that ecDNA rewires transcription not only by increasing oncogene copy number but also through associated regulatory DNA elements (Hung et al., 2021). EcDNA molecules cluster into BRD4-dependent hubs whose enhancers can act in trans on genes located either on other ecDNA molecules or on chromosomal DNA (Nichols et al., 2025), while transposable element-derived enhancers co-amplified with MYC can be reactivated on ecDNA to drive oncogene expression in cis (Kraft et al., 2025). Our findings are consistent with the broader concept that the regulatory influence of ecDNA extends beyond its own genomic locus, but reveal a mechanistically distinct mode of action. Specifically, ecDNA-derived MYC, a sequence-specific transcription factor, acts in trans at the protein level by directly activating the chromosomal target gene GPX4 through its promoter E-box. Whereas enhancer hijacking links ecDNA to increased oncogene expression, the ecMYC-GPX4 axis connects ecDNA amplification to a specific downstream effector that functions as the terminal suppressor of ferroptosis, thereby translating a structural genomic alteration into a well-defined cell death phenotype.

Our findings also refine the emerging understanding of ferroptosis in the radiation response. Seminal studies established that radiotherapy induces ferroptosis and demonstrated that ATM activation represses the cystine transporter SLC7A11, thereby limiting antioxidant capacity (Lang et al., 2019), whereas GPX4 functions as the terminal enzymatic suppressor of lipid peroxidation (Yang et al., 2014). Lei et al. reported that SLC7A11 can be adaptively

induced following irradiation, suggesting the existence of a compensatory ferroptosis-restraining program (Lei et al., 2020). Our findings support this concept of an adaptive protective mechanism but identify GPX4 as its principal effector and, importantly, define its upstream regulatory driver. Whereas previously described mechanisms are primarily based on signaling or metabolic adaptation, including ATM-SLC7A11 signaling and cystine/glutathione metabolism, we identify a structural, copy-number-based mechanism in which radiation-induced heritable ecDNA provides a sustained source of MYC that maintains GPX4 transcription. This distinction may have important clinical implications. A heritable, ecDNA-mediated increase in GPX4 expression could provide more stable and durable ferroptosis resistance than transient signaling adaptations and may help explain why certain tumors exhibit profound resistance to ferroptosis-inducing therapies. Our findings also clarify the context-dependent relationship between MYC and ferroptosis by defining a specific regulatory circuit in which ecMYC directly transactivates GPX4 in the setting of radioresistance.

These mechanistic insights also have important therapeutic implications that complement, rather than duplicate, existing ecDNA-targeted strategies. EcDNA-positive cancers have recently been shown to be selectively vulnerable to enhanced transcription–replication conflict, for example through CHK1 inhibition (Tang et al., 2024), and to depend on BET/BRD4 signaling for maintenance of ecDNA hub integrity (Hung et al., 2021). Our study identifies an additional therapeutic vulnerability based on ferroptosis. Because radioresistant cells depend on an ecDNA-driven supply of GPX4, they can be resensitized to radiotherapy either by disrupting the ecDNA compartment through BET inhibition or by directly inhibiting GPX4 with RSL3. Epistasis analysis places GPX4 downstream of ecDNA-derived MYC, establishing this regulatory hierarchy mechanistically. Combining ecDNA-targeting agents or GPX4 inhibitors with radiotherapy, therefore, represents a rational strategy for radiosensitization. Moreover, the persistent inheritance of ecMYC and COX2 expression across serial passages, consistent with the coordinated non-Mendelian inheritance of ecDNA (Hung et al., 2024), suggests that this therapeutic vulnerability is stably maintained over time.

Several limitations should be considered when interpreting these findings. First, the physical identity of the GPX4-bearing species requires further validation. Our circle sequencing analysis identified a dominant population of 250–500-bp circular DNA molecules, which falls below the resolution of current amplicon reconstruction tools, whereas large double minute-type ecDNA was demonstrated cytogenetically only for MYC. Confirmation

that GPX4 co-localizes with MYC on the same large ecDNA molecule will require whole-genome sequencing with amplicon reconstruction together with two-color metaphase FISH using GPX4 and MYC probes and a chromosome 19 control. Second, although the combination of minimal apoptosis, increased lipid peroxidation (C11-BODIPY, MDA, and 4-HNE), and pharmacological GPX4 inhibition by RSL3 strongly supports ferroptosis as the predominant mode of cell death, direct rescue experiments using ferroptosis inhibitors (Ferrostatin-1 or Liproxstatin-1) together with genetic GPX4 loss-of-function studies in the primary model would further strengthen the causal evidence. Third, the α-particle transformation model and subcutaneous xenograft model may not fully recapitulate the natural evolution of lung tumors or the complexity of the tumor microenvironment. In addition, JQ1 is a pan-BET inhibitor whose specificity, although supported by si-c-Myc experiments and MYC rescue studies, is not absolute. Finally, the clinical Raman spectroscopy cohort was relatively modest in size, warranting validation in a larger patient cohort with well-defined radiosensitive and radioresistant clinical criteria and paired analyses correlating blood-based Raman signatures with tumor GPX4 expression and ecDNA status.

In conclusion, we demonstrated that ionizing radiation induces *de novo* ecDNA formation and that ecDNA-derived MYC directly transactivates GPX4, establishing a GPX4-restrained ferroptotic state that promotes radioresistance in lung cancer. Targeting either the ecDNA compartment or GPX4 restored radiation-induced ferroptosis and improved tumor control, identifying the ecDNA-MYC-GPX4 axis as a therapeutically actionable target for radiosensitization. More broadly, our findings redefine genotoxic radiotherapy as not only a selective force acting on pre-existing ecDNA but also a direct driver of ecDNA biogenesis, providing new insight into how cancer genomes evolve under therapeutic pressure (Fig. 9). The graphical abstract is conceptually inspired by the well-known verse, “Wildfire cannot burn them away; they grow again when the spring wind blows,” symbolizing the persistence and resurgence of tumor cells despite radiation-induced damage. Mechanistically, ionizing radiation initiates ferroptosis by generating reactive oxygen species (ROS) and Fe^{2+}-dependent Fenton reactions that drive lethal lipid peroxidation. Simultaneously, radiation-induced DNA double-strand breaks are rejoined by the NHEJ machinery (DNA-PK/LIG4), generating MYC-containing ecDNA *de novo*. Following clonal selection, ecDNA-derived MYC binds the E-box within the GPX4 promoter, transcriptionally activating GPX4 expression. Elevated GPX4 detoxifies lipid peroxides, suppresses ferroptosis, and promotes radioresistance. This ecDNA-dependent resistance can be pharmacologically reversed through two complementary approaches: disruption of ecDNA transcriptional hubs

with the BRD4 inhibitor JQ1, which suppresses GPX4 transcription, or direct inhibition of GPX4 enzymatic activity with RSL3. Both strategies restore lipid ROS accumulation and reinitiate ferroptotic cell death. Collectively, these findings identify radiation-induced MYC-containing ecDNA as a key driver of ferroptosis resistance and support BRD4- or GPX4-targeted therapies as promising strategies for resensitizing residual lung cancer cells to radiotherapy.

Acknowledgments

Figures in this study was done by Biorender.

Funding Declaration

This work was supported by the National Natural Science Foundation of China (No. 82273581, and 82230108).

Author contributions

Ruixue Huang conceived the study. Ping-kun Zhou and Ruixue Huang designed the study protocol. Lihui Xuan, Jinhua Luo, Huiji Pan, and Lin Zhu performed most of the experiments. Benyang Li, Yongyi Wang, Lei Lou, and Yujie Li performed parts of the experiments. Lihui Xuan, Jinhua Luo, Huiji Pan, and Lin Zhu analyzed the data. Ting Yuan, Benyang Li, Lei Lou, and Yujie Li collected patients' blood samples. Ping-kun Zhou assisted with the critical reagents, provided technical help, and analyzed the data. Ruixue Huang assisted with Raman detection and animal study, provided technical help, analyzed the data, organized the experimental results, and prepared the figures. Ruixue Huang wrote the first draft. Ruixue Huang and Ping-kun Zhou polished the English grammar, edited, and finalized the manuscript.

Declaration of competing interests

The authors declare no competing interests.

Ethics, Consent to Participate, and Consent to Publish declarations

This study was approved by the Medical Ethics Committee of The Third Xiangya Hospital of Central South University (Approval No. 2026-S1124). All procedures involving human participants were conducted in strict accordance with the ethical guidelines of the Declaration of Helsinki. Written informed consent was obtained from all patients prior to blood sample collection.

All procedures of all animal experiments were approved by the Institutional Animal Care and Use Committee (IACUC) of Central South University (Approval No. APU-2026-0316). All animal experiments were performed in accordance with institutional guidelines. All patients provided written informed consent for the publication of their data.

During the preparation of this work, the author(s) used DeepSeek for language polishing, grammar correction, and improving the overall readability of the manuscript. The author(s) reviewed and edited the output as needed and take full responsibility for the content of the published article.

Data and code availability

The raw sequencing datasets generated in this study have been submitted to the NCBI Sequence Read Archive (SRA) database. The RNA sequencing dataset is associated with BioProject accession number PRJNA1498768 (submission ID: SUB16346335), whereas the eccDNA sequencing dataset is associated with BioProject accession number PRJNA1499291 (submission ID: SUB16348283). The datasets will be released and made publicly accessible upon acceptance and publication of this manuscript. Other data informing the results of this article will be shared upon reasonable request to the corresponding author.

References

Bailey C., Pich O., Thol K., Watkins T.B.K., Luebeck J., Rowan A., Stavrou G., Weiser N.E., Dameracharla B., Bentham R., Lu W.T., Kittel J., Yang S.Y.C., Howitt B.E., Sharma N., Litovchenko M., Salgado R., Hung K.L., Cornish A.J., Moore D.A., Houlston R.S., Bafna V., Chang H.Y., Nik-Zainal S., Kanu N., McGranahan N., Genomics England C., Flanagan A.M., Mischel P.S., Jamal-Hanjani M., Swanton C. (2024) Origins and impact of extrachromosomal DNA. Nature 635:193-200. DOI: 10.1038/s41586-024-08107-3.

Chen F., Kang R., Tang D., Liu J. (2024) Ferroptosis: principles and significance in health and disease. J Hematol Oncol 17:41. DOI: 10.1186/s13045-024-01564-3.

Hei T.K., Piao C.Q., Sutter T., Willey J.C., Suzuki K. (1996) Cellular and molecular alterations in human epithelial cells transformed by high LET radiation. Adv Space Res 18:137-48. DOI: 10.1016/0273-1177(95)00800-t.

Hung K.L., Jones M.G., Wong I.T., Curtis E.J., Lange J.T., He B.J., Luebeck J., Schmargon R., Scanu E., Bruckner L., Yan X., Li R., Gnanasekar A., Chamorro Gonzalez R., Belk J.A., Liu Z., Melillo B., Bafna V., Dorr J.R., Werner B., Huang W., Cravatt B.F., Henssen A.G., Mischel P.S., Chang H.Y. (2024) Coordinated inheritance of extrachromosomal DNAs in cancer cells. Nature 635:201-209. DOI: 10.1038/s41586-024-07861-8.

Hung K.L., Yost K.E., Xie L., Shi Q., Helmsauer K., Luebeck J., Schopflin R., Lange J.T., Chamorro Gonzalez R., Weiser N.E., Chen C., Valieva M.E., Wong I.T., Wu S., Dehkordi S.R., Duffy C.V., Kraft K., Tang J., Belk J.A., Rose J.C., Corces M.R., Granja J.M., Li R., Rajkumar U., Friedlein J., Bagchi A., Satpathy A.T., Tjian R., Mundlos S., Bafna V., Henssen A.G., Mischel P.S., Liu Z., Chang H.Y. (2021) ecDNA hubs drive cooperative intermolecular oncogene expression. Nature 600:731-736. DOI: 10.1038/s41586-021-04116-8.

Kadali V.N., Shoshani O. (2025) Aberrant nuclei with amplified DNA in cancer. Trends Cancer 11:9-11. DOI: 10.1016/j.trecan.2024.09.005.

Kang R., Liu J., Wang J., Kroemer G., Tang D. (2026) Translating ferroptosis into oncology: challenges, opportunities and future directions. Nat Rev Clin Oncol 23:401-424. DOI: 10.1038/s41571-026-01128-z.

Kim H., Nguyen N.P., Turner K., Wu S., Gujar A.D., Luebeck J., Liu J., Deshpande V., Rajkumar U., Namburi S., Amin S.B., Yi E., Menghi F., Schulte J.H., Henssen A.G., Chang H.Y., Beck C.R., Mischel P.S., Bafna V., Verhaak R.G.W. (2020) Extrachromosomal DNA is associated with oncogene amplification and poor outcome across multiple cancers. Nat Genet 52:891-897. DOI: 10.1038/s41588-020-0678-2.

Kraft K., Murphy S.E., Jones M.G., Shi Q., Bhargava-Shah A., Luong C., Hung K.L., He B.J., Li R., Park S.K., Montgomery M.T., Weiser N.E., Wang Y., Luebeck J., Bafna V., Boeke J.D., Mischel P.S., Boettiger A.N., Chang H.Y. (2025) Enhancer activation from transposable elements in extrachromosomal DNA. Nat Cell Biol 27:1914-1924. DOI: 10.1038/s41556-025-01788-6.

Lang X., Green M.D., Wang W., Yu J., Choi J.E., Jiang L., Liao P., Zhou J., Zhang Q., Dow A., Saripalli A.L., Kryczek I., Wei S., Szeliga W., Vatan L., Stone E.M., Georgiou G., Cieslik M., Wahl D.R., Morgan M.A., Chinnaiyan A.M., Lawrence T.S., Zou W.

(2019) Radiotherapy and Immunotherapy Promote Tumoral Lipid Oxidation and Ferroptosis via Synergistic Repression of SLC7A11. Cancer Discov 9:1673-1685. DOI: 10.1158/2159-8290.CD-19-0338.

Lange J.T., Rose J.C., Chen C.Y., Pichugin Y., Xie L., Tang J., Hung K.L., Yost K.E., Shi Q., Erb M.L., Rajkumar U., Wu S., Taschner-Mandl S., Bernkopf M., Swanton C., Liu Z., Huang W., Chang H.Y., Bafna V., Henssen A.G., Werner B., Mischel P.S. (2022) The evolutionary dynamics of extrachromosomal DNA in human cancers. Nat Genet 54:1527-1533. DOI: 10.1038/s41588-022-01177-x.

Lei G., Zhang Y., Koppula P., Liu X., Zhang J., Lin S.H., Ajani J.A., Xiao Q., Liao Z., Wang H., Gan B. (2020) The role of ferroptosis in ionizing radiation-induced cell death and tumor suppression. Cell Res 30:146-162. DOI: 10.1038/s41422-019-0263-3.

Liu Q., Jiang S., Xu X., Xu K., Luo Y., Yu Z., Xiang M., Xu Z., Wang L., Zhang S., Tao H., Yang X., Jiang C., Qi X., Li H., Gao Y., Li Y., Fu S., Zhou P., Bo X., Chen H., Chen X., Hu Y. (2025) TP63 mediates the generation of tumour-specific chromatin loops that underlie MYC activation in radiation-induced tumorigenesis. Nat Commun 16:8718. DOI: 10.1038/s41467-025-63754-y.

Liu X.D., Xie D.F., Wang Y.L., Guan H., Huang R.X., Zhou P.K. (2019) Integrated analysis of lncRNA-mRNA co-expression networks in the alpha-particle induced carcinogenesis of human branchial epithelial cells. Int J Radiat Biol 95:144-155. DOI: 10.1080/09553002.2019.1539880.

Nichols A., Choi Y., Norman R.X., Chen Y., Striepen J., Salataj E., Toufektchan E., Koche R., Maciejowski J. (2025) Chromosomal tethering and mitotic transcription promote ecDNA nuclear inheritance. Mol Cell 85:2839-2853 e8. DOI: 10.1016/j.molcel.2025.06.013.

Patel N.H., Sohal S.S., Manjili M.H., Harrell J.C., Gewirtz D.A. (2020) The Roles of Autophagy and Senescence in the Tumor Cell Response to Radiation. Radiat Res 194:103-115. DOI: 10.1667/RADE-20-00009.

Shoshani O., Brunner S.F., Yaeger R., Ly P., Nechemia-Arbely Y., Kim D.H., Fang R., Castillon G.A., Yu M., Li J.S.Z., Sun Y., Ellisman M.H., Ren B., Campbell P.J., Cleveland D.W. (2021) Chromothripsis drives the evolution of gene amplification in cancer. Nature 591:137-141. DOI: 10.1038/s41586-020-03064-z.

Song Y., Guan C., Zhang Y., Xu Y., Li P., Luo L., Feng C., Chen G. (2026) A novel CRISPR-Cas9 nickase-mediated rolling circle amplification (CRIRCA) technique for gene identification and quantitative analysis of extrachromosomal DNA. J Adv Res 80:239-248. DOI: 10.1016/j.jare.2025.04.031.

Tang J., Weiser N.E., Wang G., Chowdhry S., Curtis E.J., Zhao Y., Wong I.T., Marinov G.K., Li R., Hanoian P., Tse E., Mojica S.G., Hansen R., Plum J., Steffy A., Milutinovic S., Meyer S.T., Luebeck J., Wang Y., Zhang S., Altemose N., Curtis C., Greenleaf W.J., Bafna V., Benkovic S.J., Pinkerton A.B., Kasibhatla S., Hassig C.A., Mischel P.S., Chang H.Y. (2024) Enhancing transcription-replication conflict targets ecDNA-positive cancers. Nature 635:210-218. DOI: 10.1038/s41586-024-07802-5.

Wang M., Xu L., Alu A., Li P., Liu J., Chen S., He X., Han X., Yang L., Pu Q., Wei X. (2025) Integrative analysis of non-small cell lung cancer identifies Jumonji domain-containing 6/ETS homologous factor axis as a target to overcome

radioresistance. Signal Transduct Target Ther 10:391. DOI: 10.1038/s41392-025-02471-w.

Weaver D.A., Hei T.K., Hukku B., McRaven J.A., Willey J.C. (1997) Cytogenetic and molecular genetic analysis of tumorigenic human bronchial epithelial cells induced by radon alpha particles. Carcinogenesis 18:1251-7. DOI: 10.1093/carcin/18.6.1251.

Wong I.T., Yi H., Melillo B., Cravatt B.F., Chang H.Y., Mischel P.S. (2026) Targeting extrachromosomal DNA in human cancers. Nat Rev Drug Discov 25:374-389. DOI: 10.1038/s41573-025-01369-0.

Yan X., Mischel P., Chang H. (2024) Extrachromosomal DNA in cancer. Nat Rev Cancer 24:261-273. DOI: 10.1038/s41568-024-00669-8.

Yang Q.L., Xie Y., Qiao K., Lim J.Y.S., Wu S. (2025) Modern biology of extrachromosomal DNA: A decade-long voyage of discovery. Cell Res 35:11-22. DOI: 10.1038/s41422-024-01054-8.

Yang W.S., SriRamaratnam R., Welsch M.E., Shimada K., Skouta R., Viswanathan V.S., Cheah J.H., Clemons P.A., Shamji A.F., Clish C.B., Brown L.M., Girotti A.W., Cornish V.W., Schreiber S.L., Stockwell B.R. (2014) Regulation of ferroptotic cancer cell death by GPX4. Cell 156:317-331. DOI: 10.1016/j.cell.2013.12.010.

Figure legends

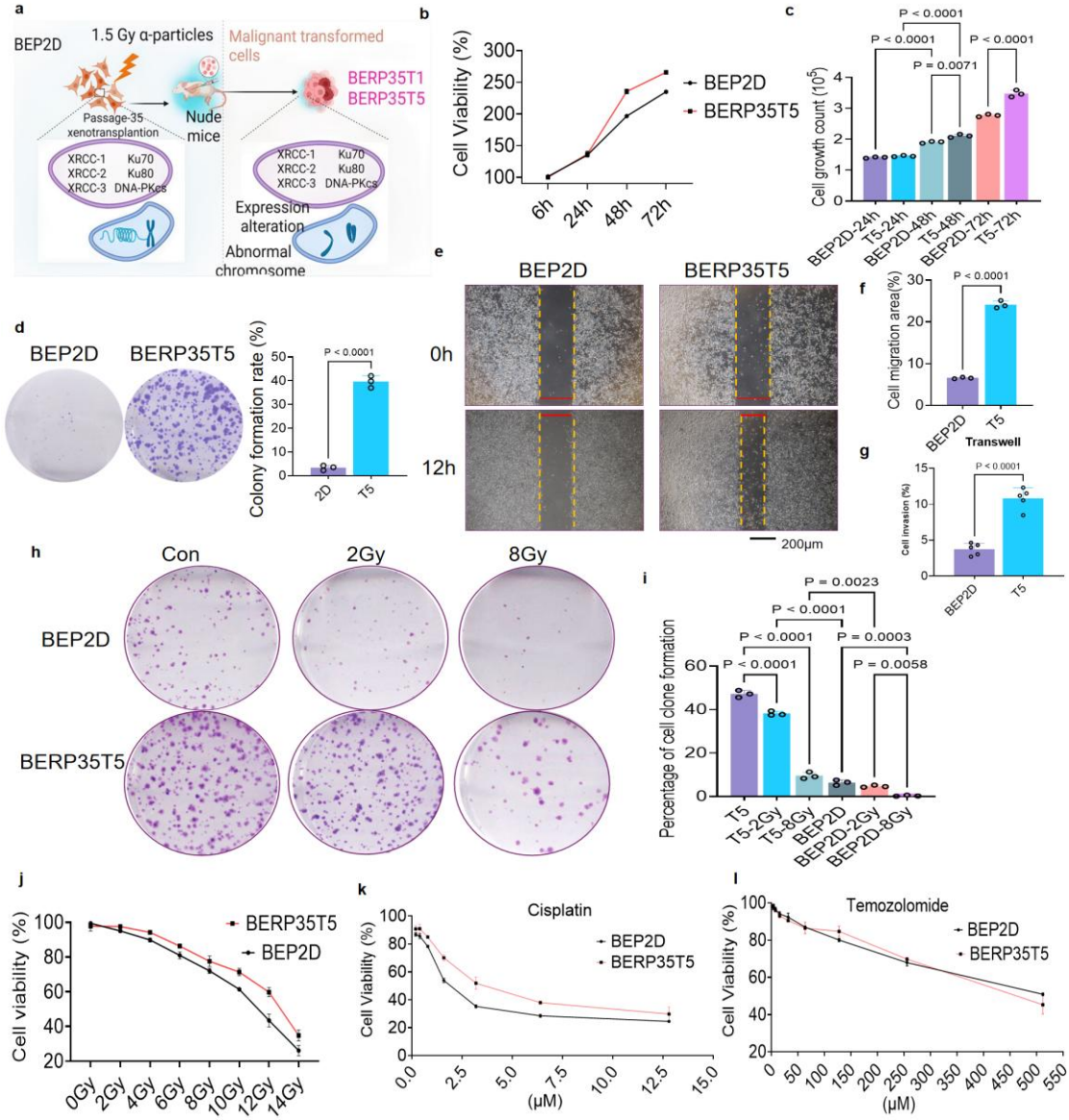


Fig. 1. Progressive α-particle-driven malignant transformation confers a radiation resistance phenotype.

(a) Schematic of the progressive malignant transformation model. The HPV18-immortalized human bronchial epithelial cell line BEP2D was exposed to 1.5 Gy α-particle irradiation from a ^{238}Pu source, followed by serial passaging and xenotransplantation into nude mice at passage 35, to generate the radiation-transformed sublines BERP35T1 (T1) and BERP35T5 (T5). The schematic also indicates altered expression of DNA damage-response factors (XRCC1, XRCC2, XRCC3, Ku70, Ku80, DNA-PKcs) and the chromosomal aberrations seen in the transformed lines. (b) Cell proliferation measured by CCK-8 assay in BEP2D and BERP35T5 cells at 6, 24, 48 and 72 h, normalized to 6 h. (c) Direct cell counting at 24, 48 and 72 h. (d) Colony formation assay in unirradiated BEP2D and BERP35T5 cells, with quantification of colony-formation rate. (e) Representative phase-contrast images of scratch wound healing at 0 and 12 h. Yellow dashed

lines indicate the wound edges. Scale bars, 200 μm. (f) Quantification of the wound-healing assay shown in (e), expressed as the percentage of wound area closed. (g) Transwell invasion assay: quantification of the percentage of invading cells in BEP2D and BERP35T5. (h) Representative colony-formation assays following exposure to 0, 2 or 8 Gy of ^{60}Co γ-rays. (i) Quantification of colony formation for the plates shown in (h). (j) Cell viability measured by CCK-8 at 72 h after exposure to 0–14 Gy irradiation. (k, l) Dose–response curves for cisplatin and temozolomide after 48 h of treatment. Data are presented as the mean ± SD from n = 3 independent experiments. Statistical significance was determined using a two-tailed Student's t test (d, f, g), one-way ANOVA with Tukey's multiple-comparison test (c, i), or two-way ANOVA (j).

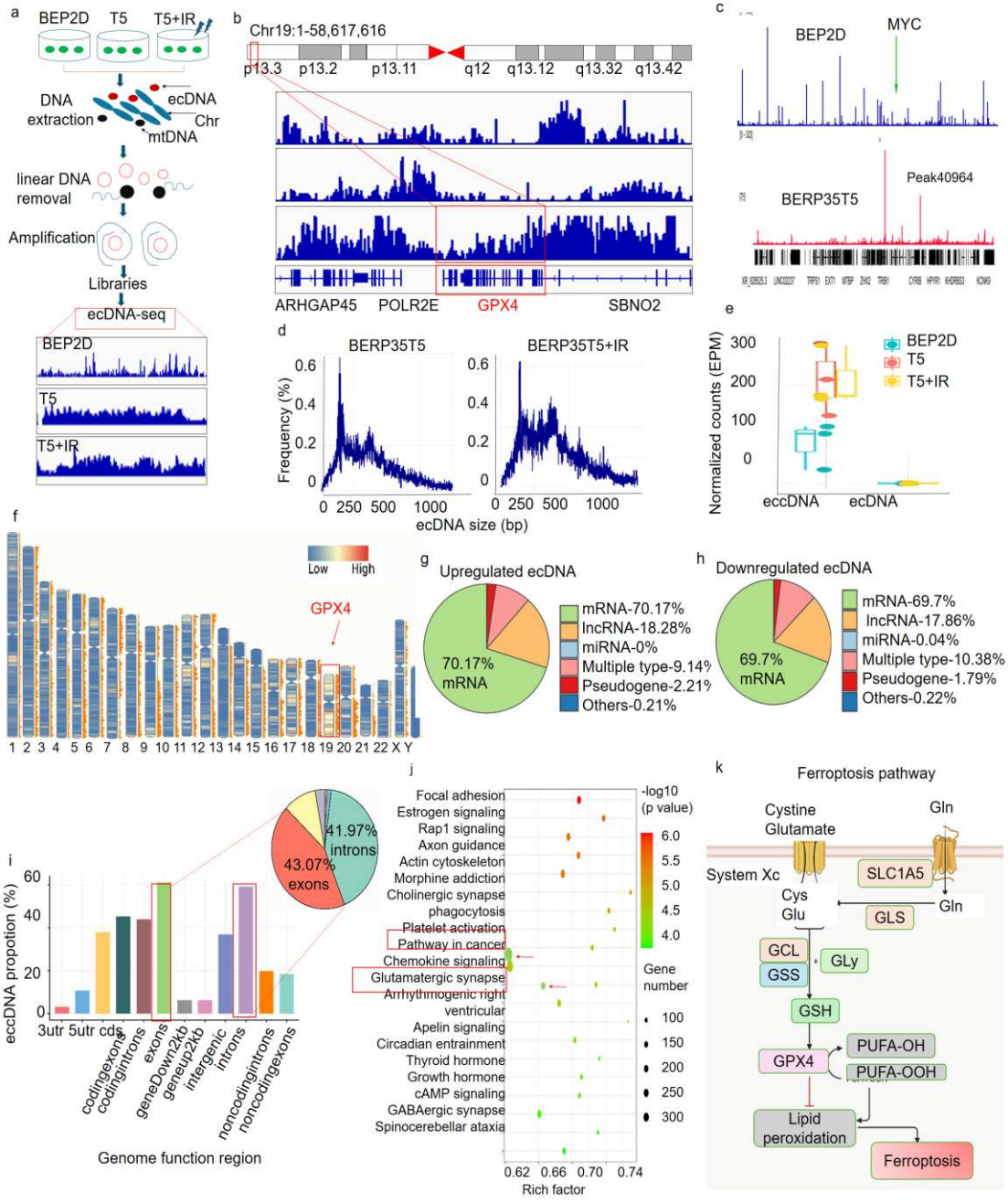


Fig. 2. Circle sequencing of BERP35T5 cells identifies radiation-associated changes in small

extrachromosomal circular DNA (eccDNA).

(a) Schematic of the circle sequencing workflow. Three groups, BEP2D, BERP35T5 (T5) and BERP35T5+IR (T5+IR; T5 cells given an additional 8 Gy of X-rays), were analysed with three biological replicates per group. Genomic DNA was enriched for circular DNA by alkaline denaturation, mitochondrial DNA was linearised with MssI, residual linear DNA was digested with Plasmid-Safe ATP-dependent DNase, and circles were amplified by φ29 rolling-circle amplification before library preparation and sequencing on Illumina NovaSeq 6000 (PE150). Circles were identified with Circle-Map using a threshold of at least two split reads together with discordant read-pair support. (b) Genome browser view of the GPX4 locus on chromosome 19 (ideogram, chr19:1–58,617,616), showing circular DNA coverage in BEP2D, BERP35T5 and BERP35T5+IR. The gene order in the window is ARHGAP45–POLR2E–GPX4–SBNO2.(c) Genome browser view of the chromosome 8q24 region containing MYC in BEP2D and BERP35T5 cells. (d) Size distribution of circular DNA molecules in BERP35T5 and BERP35T5+IR cells; x-axis, circle size (bp); y-axis, frequency (%). In both groups the molecules were predominantly [150–500] bp. (e) Box plots of normalised circle counts (EPM) in BEP2D, T5 and T5+IR cells, separated into eccDNA and ecDNA categories. (f) Genome-wide chromosomal distribution of circular DNA. Chromosome ideograms (1–22, X, Y) are coloured from low (blue) to high (red) circle density; the GPX4 locus on chromosome 19 is boxed. (g, h) Pie charts of the biotype annotation of differentially abundant circles in BERP35T5+IR versus BERP35T5. (g) Upregulated: mRNA 70.17%, lncRNA 18.28%, miRNA 0%, multiple biotypes 9.14%, pseudogenes 2.21%, others 0.21%. (h) Downregulated: mRNA 69.70%, lncRNA 17.86%, miRNA 0.04%, multiple biotypes 10.38%, pseudogenes 1.79%, others 0.22%. (i) Distribution of circular DNA across genomic feature categories, with the inset pie chart showing the exon (43.07%) and intron (41.97%) fractions.(j) KEGG pathway enrichment analysis of genes associated with upregulated circles in BERP35T5+IR versus BERP35T5 cells. The x-axis is the rich factor, bubble size the number of enriched genes, and colour the significance (−log10 P value). (k) Proposed model of the ferroptosis pathway. The system Xc^- antiporter mediates cystine/glutamate exchange; intracellular cystine is reduced to cysteine while glutaminase (GLS) converts glutamine to glutamate, both feeding glutathione (GSH) synthesis. GPX4 uses GSH to reduce phospholipid hydroperoxides (PUFA-OOH) to the corresponding alcohols, suppressing lipid peroxidation and ferroptosis. MYC encoded on ecDNA drives GPX4 transcription (Fig. 6), raising GPX4 protein and thereby conferring resistance to radiation-induced ferroptosis.

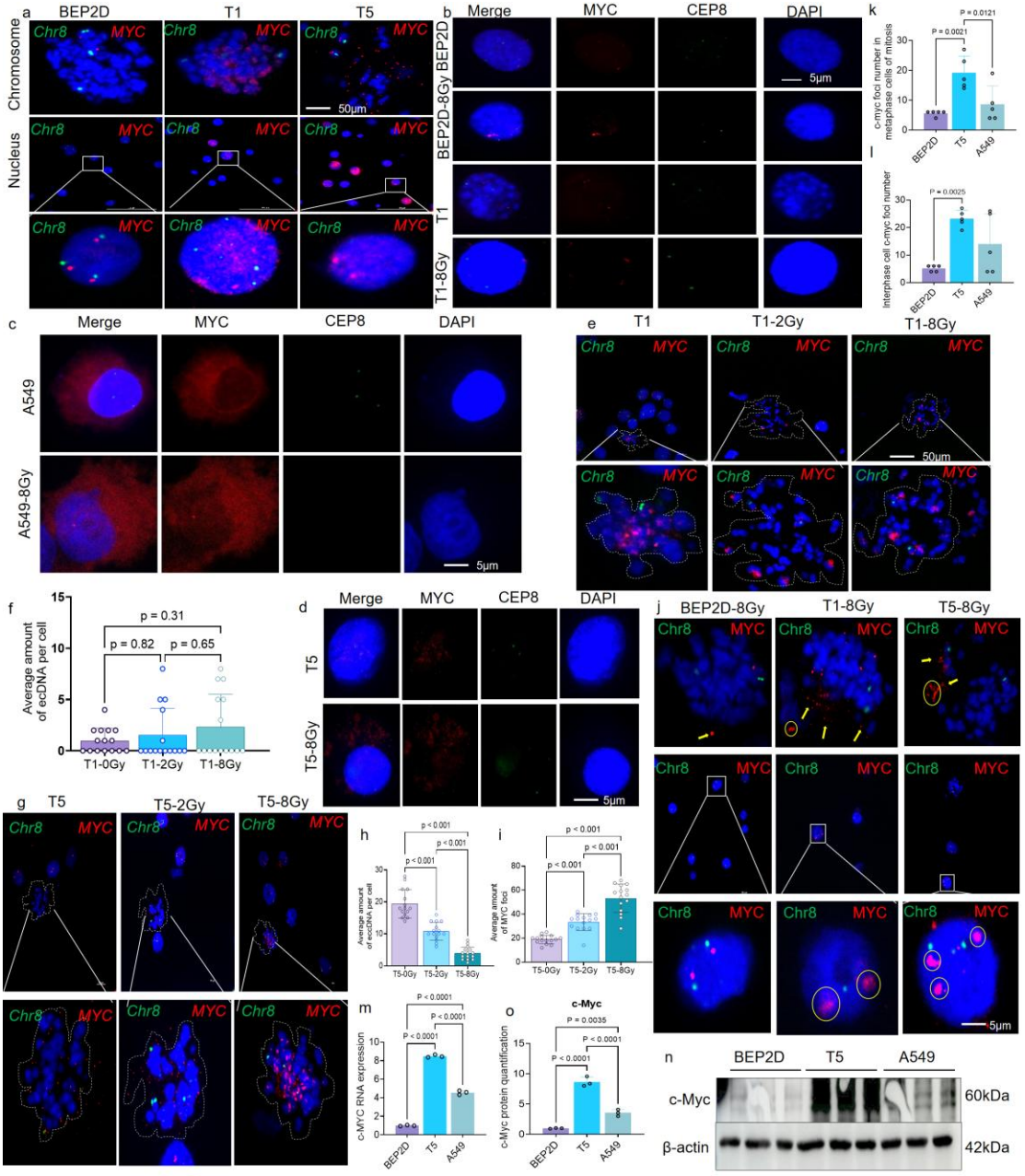


Fig. 3. Radiation-induced MYC amplification in transformed BEP2D cells is extrachromosomal and increases with dose in T5 cells.

(a) Two-color DNA FISH for MYC (red) and a chromosome 8 centromere probe (CEP8; green),

with DAPI counterstaining (blue), in parental BEP2D cells and the radiation-transformed clones T1 and T5. Upper panels show metaphase spreads and lower panels interphase nuclei; boxed regions are enlarged below. In BEP2D, MYC signals are few and colocalize with CEP8; in T1 and T5 they are numerous, dispersed and spatially separated from CEP8. Scale bar, 50 μm. (b–d) Representative channel-split DNA FISH images (Merge, MYC, CEP8, DAPI) before and after 8 Gy irradiation in (b) BEP2D and T1 cells, (c) A549 cells and (d) T5 cells. Scale bar, 5 μm. (e) Representative MYC/CEP8 DNA FISH images of T1 cells exposed to 0, 2 or 8 Gy. Upper panels, interphase nuclei; lower panels, metaphase spreads (dashed outlines). Scale bar, 50 μm.(f)

Quantification of total MYC-positive extrachromosomal foci per cell in T1 cells after 0, 2 or 8 Gy. No significant differences were detected (P = 0.31, 0.82 and 0.65). (g) Representative MYC/CEP8 DNA FISH images of T5 cells after 0, 2 or 8 Gy. Scale bar, 50 μm. (h) Quantification of average amount of eccDNA per cell in T5 cells, showing a dose-dependent decrease (0 vs 2 vs 8 Gy; all $P < 0.001$). (i) Quantification of MYC foci per cell in T5 cells, showing a dose-dependent increase (0 vs 2 vs 8 Gy; all $P < 0.001$). (j) Representative MYC/CEP8 metaphase DNA FISH images of BEP2D, T1 and T5 cells after 8 Gy. Arrows and circles indicate extrachromosomal MYC signals; boxed regions are enlarged below. Scale bar, 5 μm. (k) Quantification of MYC foci per metaphase spread in BEP2D, T5 and A549 cells (BEP2D vs T5, P = 0.0021; T5 vs A549, P = 0.0121). (l) Quantification of MYC foci per interphase nucleus in BEP2D, T5 and A549 cells.(m) Relative MYC mRNA expression by RT-qPCR in BEP2D, T5 and A549 cells (all pairwise comparisons, $P < 0.0001$).(n) Representative immunoblot of c-MYC (~60 kDa) with β-actin (~42 kDa) as loading control in BEP2D, T5 and A549 cells (three biological replicates per line).(o) Densitometric quantification of (n), normalized to β-actin (BEP2D vs T5, $P < 0.0001$; BEP2D vs A549, P = 0.0035; T5 vs A549, $P < 0.0001$).Data are presented as the mean ± SD.

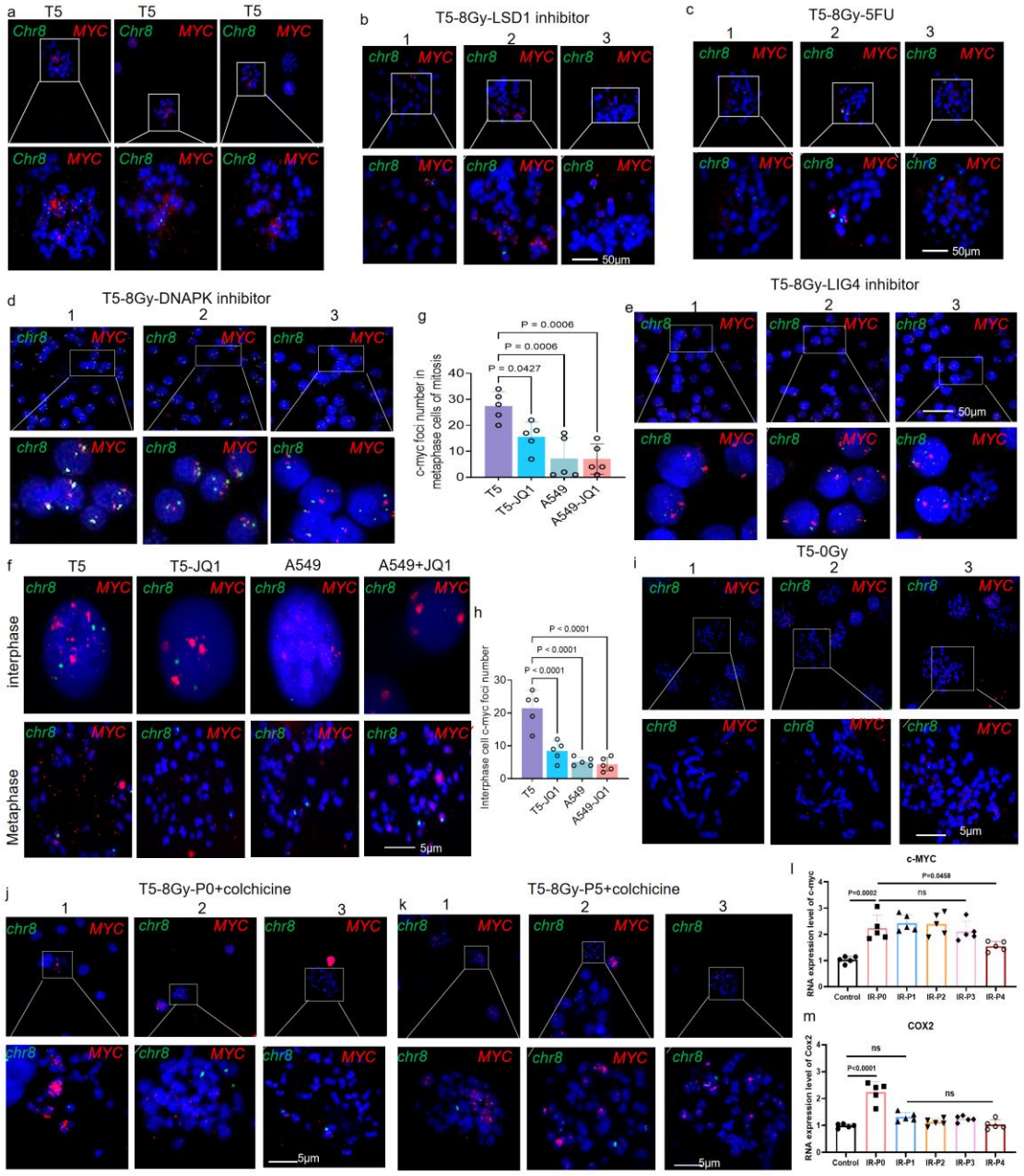


Fig. 4. Radiation-induced ecMYC formation depends on BET/BRD4 activity, and is heritable.

(a) Representative MYC/CEP8 DNA FISH images of vehicle-treated T5 cells (three fields).(b) T5 cells exposed to 8 Gy and treated with an LSD1 inhibitor (three fields). Scale bar, 50 μm.(c) T5 cells exposed to 8 Gy and treated with 5-fluorouracil (three fields). Scale bar, 50 μm.(d) T5 cells exposed to 8 Gy and treated with a DNA-PK inhibitor (three fields).(e) T5 cells exposed to 8 Gy and treated with a LIG4 inhibitor (three fields). Scale bar, 50 μm.(f) Representative interphase and metaphase DNA FISH images of T5 and A549 cells treated with or without JQ1. MYC, red; CEP8, green; DAPI, blue. Scale bar, 5 μm.(g) Quantification of MYC foci per metaphase spread in T5, T5+JQ1, A549 and A549+JQ1 (T5 vs T5+JQ1, P = 0.0427; T5 vs A549, P = 0.0006; T5 vs A549+JQ1, P = 0.0006).(h) Quantification of MYC foci per interphase nucleus in the same four

groups (all P < 0.0001). (i) Representative DNA FISH images of unirradiated T5 cells (three fields). Scale bar, 5 μm.(j, k) Representative DNA FISH images of colcemid-arrested T5 cells after 8 Gy at passage 0 (j) and passage 5 (k). Arrows and clustered signals indicate ecMYC. Scale bar, 5 μm. (l) Relative MYC mRNA expression in control and irradiated cells across serial passages (IR-P0 to IR-P4).(m) Relative COX2 (PTGS2) mRNA expression in the same samples.

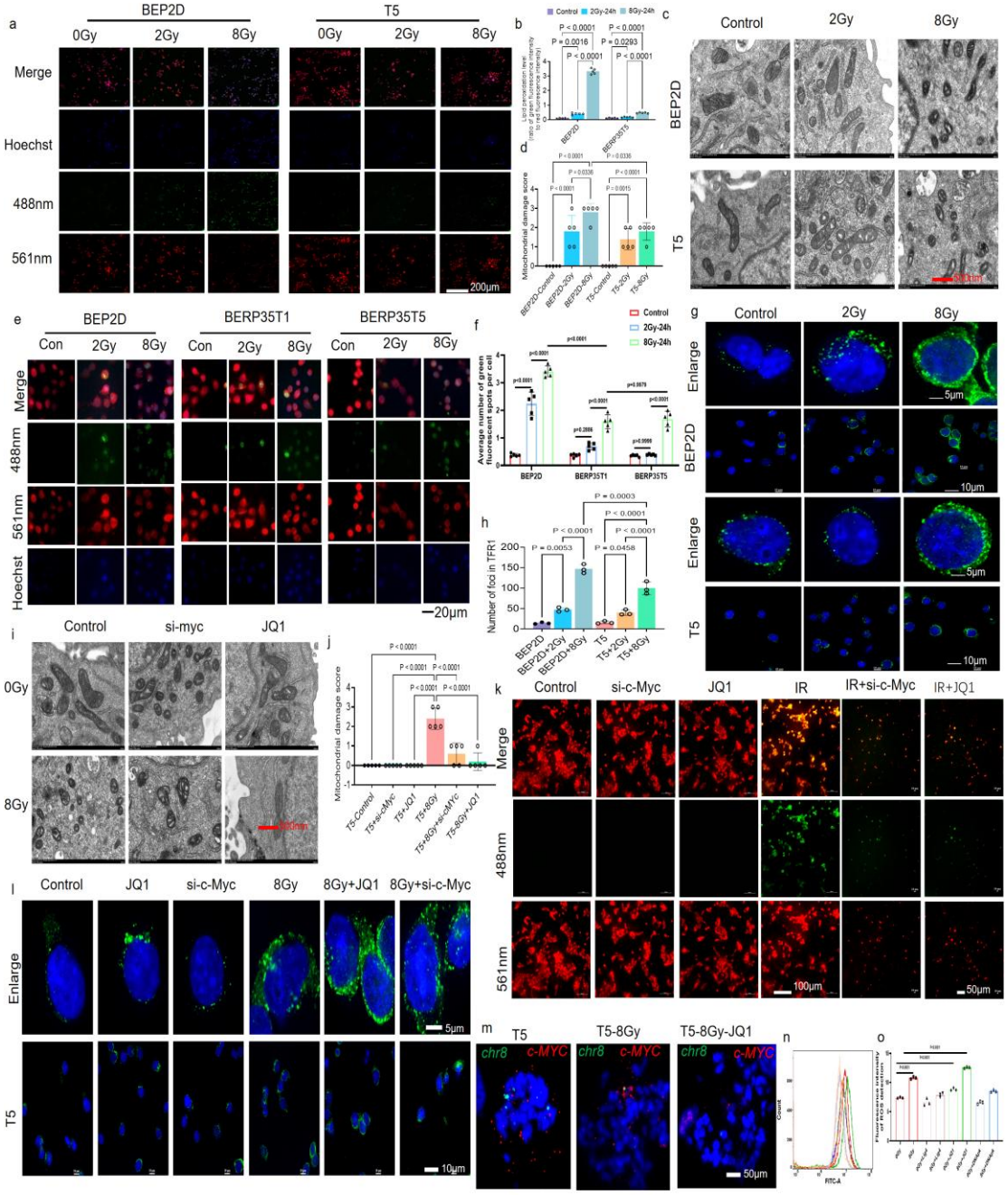


Fig. 5. Radiation induces lipid peroxidation and ferroptotic ultrastructural damage, and disruption of ecDNA signalling modifies the ferroptotic response.

(a) Representative fluorescence images of lipid peroxidation measured with the C11-BODIPY

581/591 probe in BEP2D and T5 cells 24 h after 0, 2 or 8 Gy irradiation. Rows show the merged image, Hoechst (nuclei), the 488 nm channel (oxidised probe) and the 561 nm channel (reduced probe). Scale bar, 200 um. **(b)** Quantification of (a), expressed as the ratio of 488 nm (oxidised) to 561 nm (reduced) fluorescence intensity, in BEP2D and BERP35T5 cells at 24 h (Control, 2 Gy-24 h, 8 Gy-24 h). Lipid peroxidation increased with dose in both lines, and the increase was substantially larger in BEP2D than in BERP35T5 cells. P values as indicated in the panel.**(c)** Representative transmission electron micrographs of BEP2D and T5 cells 24 h after 0 (Control), 2 or 8 Gy irradiation, showing the ultrastructural features of ferroptosis: mitochondrial shrinkage, increased outer-membrane density and loss of cristae. Scale bar, 500 nm. **(d)** Mitochondrial damage score derived from the micrographs in (c) for BEP2D-Control, BEP2D-2Gy, BEP2D-8Gy, T5-Control, T5-2Gy and T5-8Gy. P values as indicated.**(e)** Representative high-magnification C11-BODIPY images of BEP2D, BERP35T1 and BERP35T5 cells 24 h after 0 (Con), 2 or 8 Gy irradiation. Rows show the merged image, the 488 nm channel (oxidised probe), the 561 nm channel (reduced probe) and Hoechst. Scale bar, 20 um.**(f)** Quantification of (e), expressed as the average number of green (oxidised-probe) fluorescent puncta per cell, across the three cell lines and three doses (Control, 2 Gy-24 h, 8 Gy-24 h). P values as indicated. **(g)** Representative immunofluorescence images of TFR1 (green) with Hoechst counterstain (blue) in BEP2D and T5 cells 24 h after 0 (Control), 2 or 8 Gy irradiation. For each cell line the upper row shows enlarged single cells and the lower row the corresponding field. Scale bars, 5 um (enlarged) and 10 um (field). **(h)** Quantification of (g), expressed as the number of TFR1 foci per cell, for BEP2D, BEP2D+2Gy, BEP2D+8Gy, T5, T5+2Gy and T5+8Gy ($P = 0.0003$, < 0.0001, $= 0.0053$, $= 0.0458$ and as indicated in the panel). **(i)** Representative transmission electron micrographs of T5 cells treated with [control siRNA], si-c-Myc or JQ1 and either left non-irradiated (0 Gy) or irradiated (8 Gy), examined at time point as indicated. Scale bar, 500 nm. **(j)** Mitochondrial damage score derived from (i) for T5-Control, T5+si-c-Myc, T5+JQ1, T5+8Gy, T5+8Gy+si-c-Myc and T5+8Gy+JQ1 ($P < 0.0001$ for the comparisons indicated). **(k)** Representative C11-BODIPY images of T5 cells under six conditions: Control, si-c-Myc, JQ1, IR (8 Gy), IR+si-c-Myc and IR+JQ1. Rows show the merged image, the 488 nm channel (oxidised probe) and the 561 nm channel (reduced probe). Scale bars, 100 um and 50 um. **(l)** Representative TFR1 immunofluorescence (green) with Hoechst counterstain (blue) in T5 cells under six conditions: Control, JQ1, si-c-Myc, 8 Gy, 8 Gy+JQ1 and 8 Gy+si-c-Myc. Upper row, enlarged single cells; lower row, the corresponding field. Scale bars, 5 um and 10 um. **(m)** Representative DNA FISH images of T5, T5-8Gy and T5-8Gy-JQ1 cells showing the chromosome 8 centromere (chr8, green) and c-MYC (red). Scale bars, 50 um and 10 um. **(n)** Representative flow cytometry histograms of C11-BODIPY fluorescence (FITC channel) for the indicated treatment groups. **(o)** Quantification of the flow cytometry data in (n) across the eight groups indicated. P values as shown in the panel. Data are presented as mean ± SD from 3 independent experiments. Statistical tests are specified in the Methods; exact P values are shown in the corresponding panels.

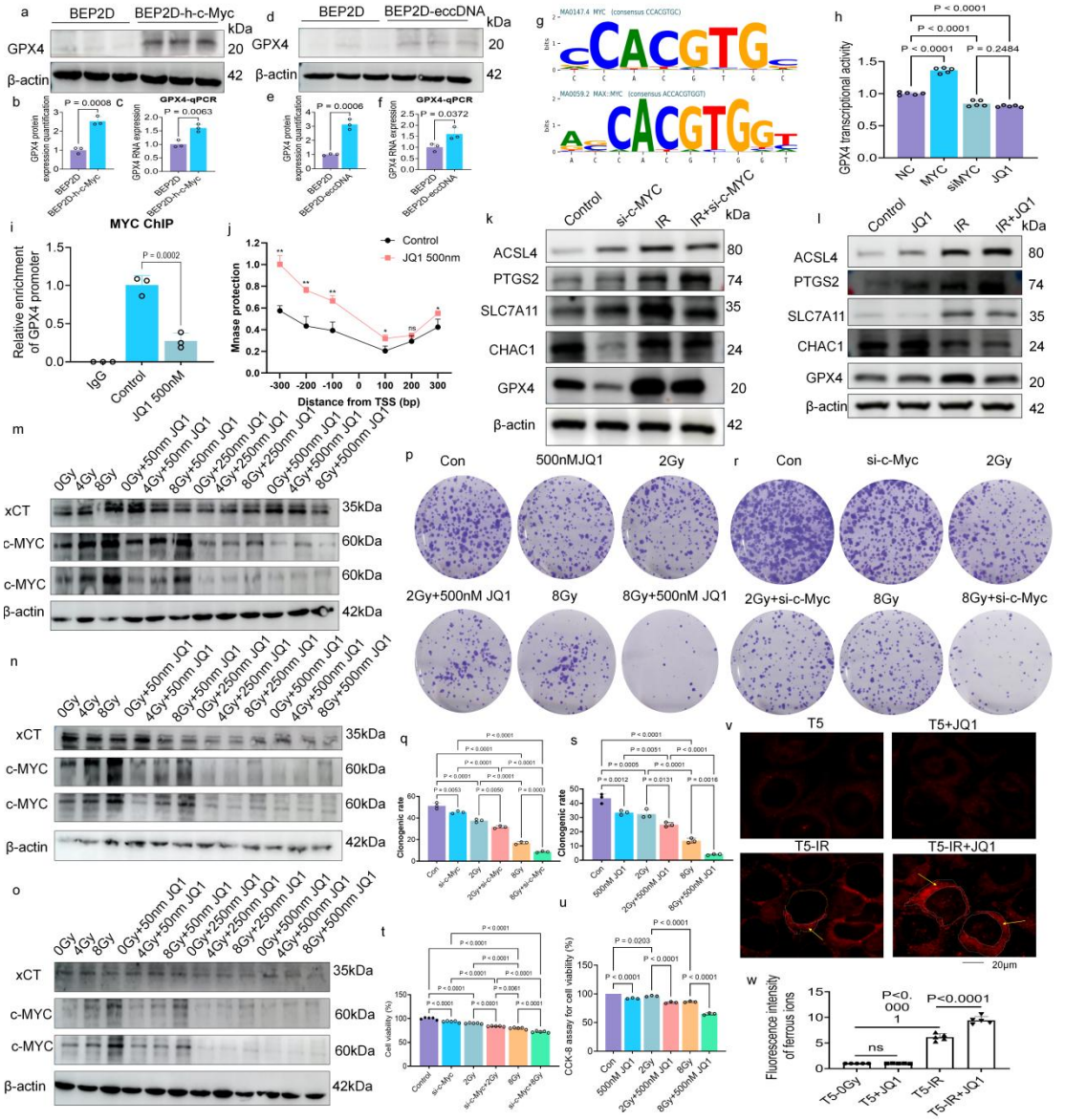


Fig. 6. ecDNA-derived MYC transcriptionally activates GPX4 to promote ferroptosis resistance.

(a) Representative immunoblot of GPX4 in BEP2D and BEP2D-h-c-Myc cells (BEP2D overexpressing human c-MYC). β-actin, loading control. (b) Densitometric quantification of (a) (P = 0.0008). (c) Relative GPX4 mRNA by RT-qPCR in BEP2D and BEP2D-h-c-Myc cells (P = 0.0063). (d) Representative immunoblot of GPX4 in BEP2D and BEP2D-eccDNA cells. (e) Densitometric quantification of (d) (P = 0.0006).(f) Relative GPX4 mRNA by RT-qPCR in the same cells (P = 0.0372). (g) Predicted MYC-binding motifs: JASPAR MA0147.4 (MYC; consensus CCACGTGC) and MA0059.2 (MAX::MYC; consensus ACCACGTGGT). The GPX4 promoter contains a canonical E-box (CACGTG). (h) GPX4 promoter reporter activity in cells transfected with negative control (NC), MYC or si-MYC, or treated with JQ1 (NC vs MYC, P < 0.0001; NC vs siMYC, P < 0.0001; siMYC vs JQ1, P = 0.2484). (i) MYC ChIP-qPCR at the GPX4 promoter in control and JQ1-treated (500 nM) cells, with an IgG control (control vs JQ1, P

= 0.0002). (j) MNase protection assay across the GPX4 promoter (−300 to +300 bp relative to the transcription start site) in control and JQ1-treated cells.(k) Immunoblots of ACSL4, PTGS2, SLC7A11 and CHAC1 and of GPX4 in Control, si-c-MYC, IR and IR+si-c-MYC cells; β-actin, loading control.(l) Immunoblots of the same proteins in Control, JQ1, IR and IR+JQ1 cells.(m–o) Immunoblots of xCT (SLC7A11), c-MYC and β-actin across the indicated radiation doses and JQ1 concentrations. (p, q) Representative colony-formation plates and quantification of clonogenic rate in T5 cells treated with 500 nM JQ1 with or without 2 or 8 Gy. (r, s) The equivalent colony-formation experiment using si-c-Myc, with quantification. (t, u) Cell viability (CCK-8) under the corresponding JQ1 and si-c-Myc conditions.(v) Representative ferrous-iron probe fluorescence images of T5, T5+JQ1, T5-IR and T5-IR+JQ1 cells. Scale bar, 20 μm.(w) Quantification of ferrous-iron fluorescence intensity (T5-0Gy vs T5-JQ1, not significant; T5-IR, P < 0.0001; T5-IR+JQ1, P = 0.0001).

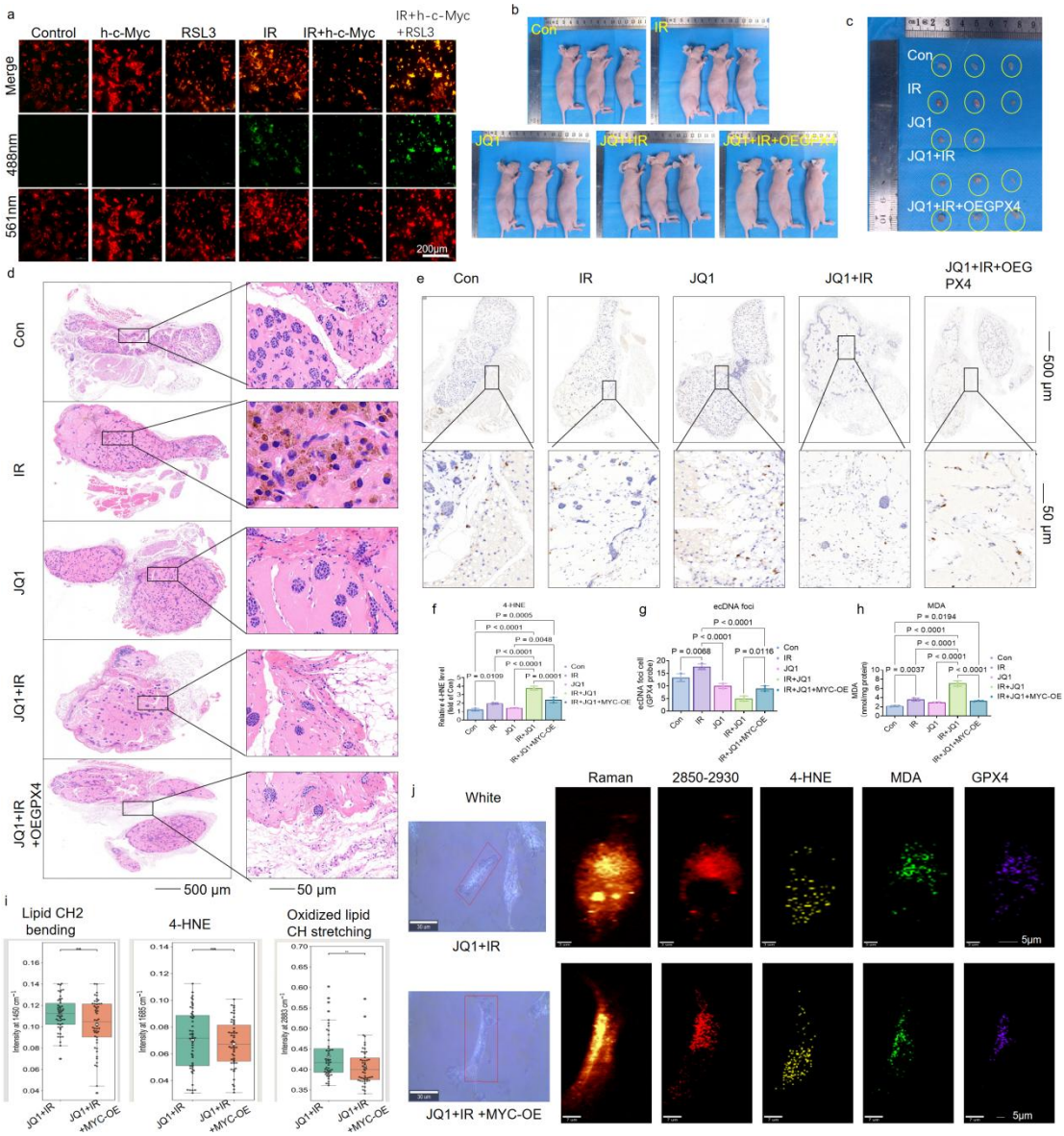


Fig. 7. Targeting ecDNA restores radiation-induced ferroptosis and tumor control in vivo, and Raman spectroscopy detects the resulting shift in lipid oxidation.

(a) Representative C11-BODIPY images of lipid ROS in T5 cells under six conditions: Control, h-c-Myc, RSL3, IR (8 Gy), IR + h-c-Myc and IR + h-c-Myc + RSL3. Rows: merge, oxidized channel (488 nm), reduced channel (561 nm). Ectopic c-MYC suppressed radiation-induced probe oxidation and RSL3 abolished this protection, placing GPX4 functionally downstream of MYC. Scale bar, 200 μm.(b) Representative images of nude mice bearing subcutaneous T5 xenografts at endpoint. Five groups: Con, IR, JQ1, JQ1 + IR, JQ1 + IR + OEGPX4. n = 3 mice per group. (c) Representative images of excised tumors from the five groups.(d) Representative haematoxylin and eosin-stained tumor sections. Left, whole sections; right, higher magnification of the boxed regions. Scale bars, 500 μm and 50 μm.(e) Representative immunohistochemical staining for MDA in tumor sections from the five groups. Upper, whole sections; lower, higher magnification. DAB, brown; haematoxylin counterstain, blue. Scale bars, 500 μm and 50 μm.(f) Quantification of intratumoral 4-HNE across the five groups. (g) Quantification of GPX4 locus-associated ecDNA foci per cell by DNA FISH in tumor sections.(h) Quantification of intratumoral MDA (nmol mg^{-1} protein) in the five groups.(i) Label-free Raman analysis of individual T5 cells after JQ1 + IR or JQ1 + IR + OEGPX4. Box plots, left to right: the lipid CH_2 bending band (1440–1450 cm^{-1}; total lipid content), the carbonyl/C=C band (~1650–1740 cm^{-1}) used as a label-free surrogate for 4-HNE, and the intensity at 2883 cm^{-1}. Statistical significance was determined using a two-tailed Mann-Whitney U test. (j) Representative confocal Raman images of the two groups in (i). Upper row, JQ1 + IR; lower row, JQ1 + IR + OEGPX4. Columns, left to right: white-light image with the mapped region outlined in red, total Raman intensity, the C–H stretching band (2850–2930 cm^{-1}), the 4-HNE map, the MDA map and the GPX4 map. Images within each column were acquired and displayed using identical settings. Scale bar, 5 μm.

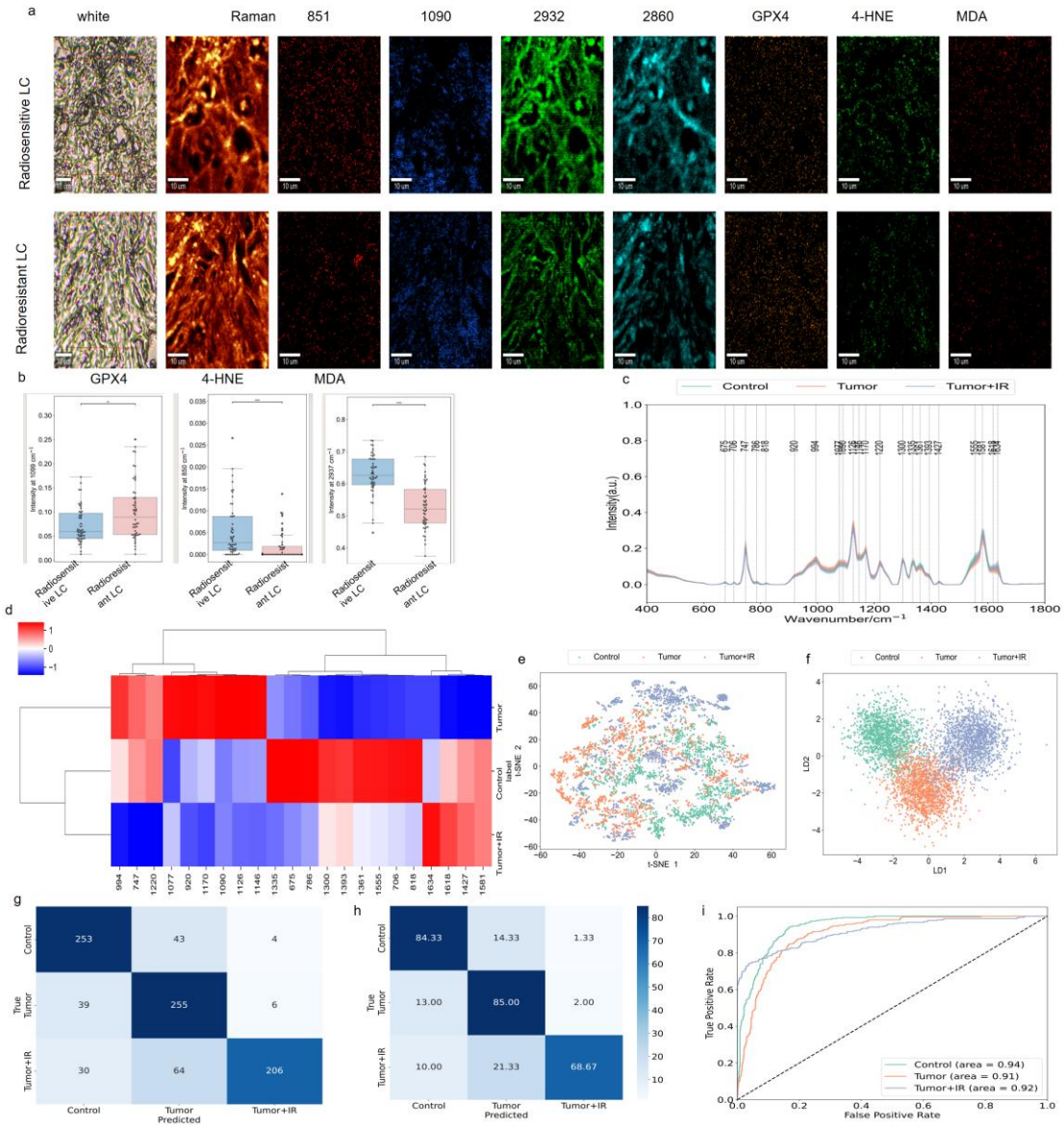


Fig. 8. Raman analysis links oxidative-lipid status to radiation response in human lung tumors and discriminates erythrocyte spectra from patients with lung cancer.

(a) Representative confocal Raman maps and matched images of radiosensitive (top) and radioresistant (bottom) human lung cancer (LC) specimens. Columns, left to right: white-light image; total Raman intensity; single-band maps at 851 cm^{-1} (proline/hydroxyproline ring breathing, collagen-associated), 1090 cm^{-1} (PO_2^- symmetric stretch, nucleic acids and phospholipids), 2932 cm^{-1} (protein CH_3 stretch) and 2860 cm^{-1} (lipid CH_2 symmetric stretch); and GPX4, 4-HNE and MDA on serial sections imaged in the matched tumor region. Scale bars, 10 μm. **(b)** Quantification in radiosensitive versus radioresistant tumors of Raman band intensities at 1099, 850 and 2937 cm^{-1} / GPX4, 4-HNE and MDA staining intensity. Boxes, median and IQR; whiskers, 1.5 × IQR.; **P < 0.01, ****P < 0.0001.**(c)** Mean label-free

Raman spectra (400–1800 cm^{-1}) of peripheral-blood erythrocytes from healthy controls (Control), patients with lung cancer (Tumor) and patients after radiotherapy (Tumor + IR). Dashed lines mark the bands entered into the statistical analysis. Spectra were regions outside fitted peaks are zero-valued by construction. n = 85 donors (Control 27, Tumor 28, Tumor + IR 30); 4,150 single-cell spectra.**(d)** Clustered heatmap of group-mean intensities for the significantly different bands, z-scored across the three groups (−1 to 1), with hierarchical clustering of bands. **(e)** Unsupervised t-SNE of erythrocyte Raman spectra; the three groups overlap substantially.**(f)** Supervised linear discriminant analysis of the same spectra; separation was validated by permutation testing and by projection of held-out donors.**(g, h)** Confusion matrices for the best-performing MLP classifier on the independent test set (n = 18 donors, 6 per group; 300 spectra per group), shown as counts (g) and row percentages (h).**(i)** One-vs-rest ROC curves for the same classifier at the single-spectrum level.

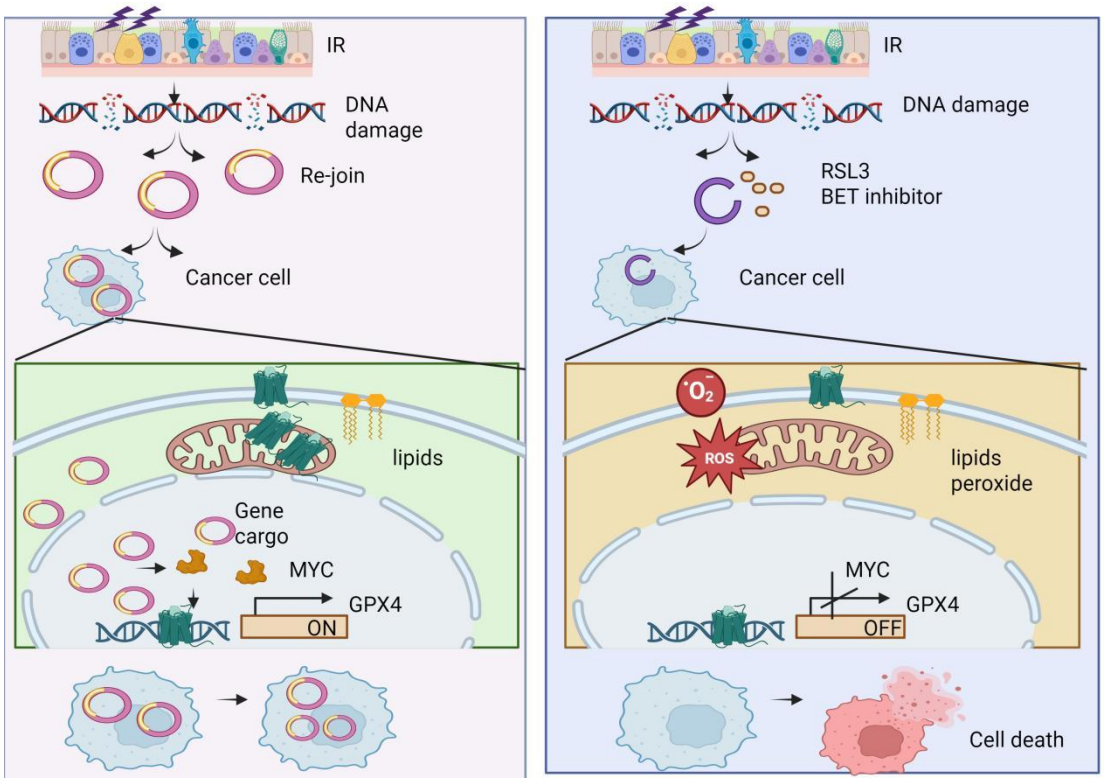


Fig. 9. Working model of the ecDNA-MYC-GPX4 axis underlying ferroptosis-resistant radioresistance.

Left panel, ionizing radiation induces DNA double-strand breaks that undergo aberrant repair and religation through the NHEJ pathway, resulting in de novo formation of MYC-containing ecDNA.The resulting ecDNA is inherited by transformed cells and serves as a source of MYC, which binds the E-box within the GPX4 promoter and activates GPX4 transcription. Elevated GPX4 reduces phospholipid hydroperoxides, suppresses lipid peroxidation, and enables tumor cells to survive radiation-induced oxidative membrane damage. Because ecDNA lacks

centromeres it segregates randomly at mitosis, generating marked cell-to-cell heterogeneity in copy number; selection under radiation then enriches for high-copy cells, sustaining the radioresistant phenotype.Right panel, pharmacological disruption of this pathway restores ferroptosis sensitivity. BET bromodomain inhibition disrupts BRD4-dependent ecDNA transcriptional hubs and suppresses MYC expression, whereas direct GPX4 inhibition with RSL3 blocks GPX4 enzymatic activity. Both interventions permit accumulation.

Supplementary Files

This is a list of supplementary files associated with this preprint. Click to download.

- Supplementaryinformationfiguresandtables.docx
- Supplementaryfileuncroppedgelsandblots.docx